ADVANCED ENGINEERING MATERIALS
www.aem-journal.com

Thermo-Mechanical Study on Auxetic Shape Memory Periodic Open Cellular Structures—Part I: Characterization of Reentrant Geometry and Effective Heat Conductivity

*Dominik Rudolf, Alexander Fink, Carolin Körner, and Hannsjörg Freund**

Periodic open cellular structures (POCS) are additively manufactured supports for heterogeneous catalysts in the field of chemical reaction engineering. Constructed from a repeated unit cell, POCS offer excellent heat transport characteristics due to heat conduction in the continuous solid matrix. However, when inserted into tubular reactors, a loose fit between structure and tube wall results. This considerably hinders heat transfer across the wall. The novel POCS concept presented in this work aims at an intensified wall heat transfer by utilizing a reentrant structure design to ensure auxetic behavior. If the POCS is made of shape memory alloy, it can recover its original shape. Combining these two effects with an initial radial oversize, an interference fit with the tube is established. This contribution comprises the geometric description of reentrant POCS and heat conduction simulations for characterization of the effective heat conductivity, yielding scaling correlations dependent on geometric parameters. Moreover, the effective radial heat conductivity of POCS in cylindrical shape is explicitly investigated. The influencing factor identified is the ratio of tube diameter and cell size: while the ratio increases, the effective radial heat conductivity decreases, but remains well above the effective heat conductivity of the unit cell.

1. Introduction

Additive manufacturing unlocks new degrees of freedom in the design and production of tailor-made components and cellular materials.[1] The design flexibility of additive manufacturing is utilized in the research field of process engineering by producing novel structures, such as periodic open cellular structures (POCS).[2] These are grid-like lattices that are built up from a characteristic unit cell, see **Figure 1**, repeated in the three spatial directions. This way, POCS facilitate systematic investigations based on geometric and material parameters (experimental) as well as on the representative unit cell (simulative). Moreover, POCS offer a high potential of target-oriented optimization. Thus, POCS have gained huge interest in chemical engineering over the last decade.[3] Made from metal alloys, POCS offer great potential for process intensification, as they feature a high effective heat conductivity due to the continuous solid matrix.[4] As such, they are exceptionally suited to serve as structured catalyst carriers, i.e., with catalytic coating, or as a hybrid system, called "packed POCS," where conventional catalyst pellets fill the void of POCS.[5,6] Either way, POCS have proven to enable an enhanced heat management in chemical reactors with heat transfer across the tube wall.[7–10] Moreover, due to their design flexibility POCS are considered an emerging opportunity compared to earlier and more mature research topics on structured catalysts and reactors. Dominant previous examples are monolithic honeycombs (mainly exhaust gas treatment applications) and highly porous, irregular open-cell foam structures, where the latter can be described as a negative image of a packed particle bed. However, monolithic honeycombs do not allow for lateral mixing of flowing reactants, whereas foam structures are restricted in possibilities for geometric optimization.[11]

Previous fundamental studies on the effective heat conductivity of POCS are based on 3D simulations of heat conduction through the solid material.[12–14] The influence of any arbitrary fluid is commonly neglected since a general characterization of these structures as cellular metamaterials is addressed, or for the case that the heat conductivity of the fluid is negligibly low, as in the case of gas phase applications. Regarding the term POCS in a broader sense, more specific studies take into account

D. Rudolf, H. Freund
Department of Biochemical and Chemical Engineering
Institute of Reaction Engineering and Catalysis
TU Dortmund University
Emil-Figge-Strasse 66, 44227 Dortmund, Germany
E-mail: hannsjoerg.freund@tu-dortmund.de

A. Fink
Joint Institute of Advanced Materials and Processes
Friedrich-Alexander Universität Erlangen-Nürnberg
Dr.-Mack-Strasse 81, 90762 Fürth, Germany

C. Körner
Chair of Materials Science and Engineering for Metals
Friedrich-Alexander Universität Erlangen-Nürnberg
Martensstrasse 5, 91058 Erlangen, Germany

The ORCID identification number(s) for the author(s) of this article can be found under https://doi.org/10.1002/adem.202401717.

DOI: 10.1002/adem.202401717

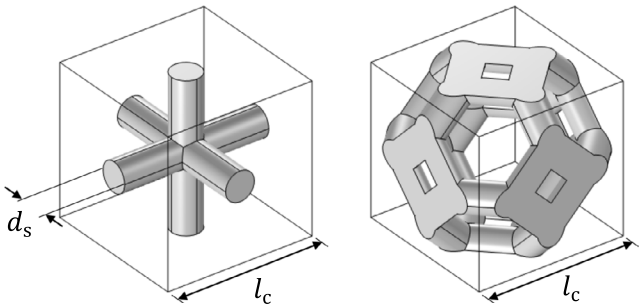

Figure 1. Two exemplary isotropic unit cells with strut diameter d_s and cell size l_c: the cubic unit cell (left) and the Kelvin unit cell (right).

the influence of a fluid on the stagnant effective heat conductivity, considering potential applications in the electrochemical and mobility sector or for thermal energy storage.[15,16] Models for the calculation of the effective heat conductivity of porous, mostly irregular cellular materials are extensively researched. Such models are required for an accurate dimensioning and optimization of porous components for various heat transfer applications. Many models are available in the literature, for example, listed in an extensive review regarding the effective heat conductivity of metal foams by Ranut.[17] Generally, there are three different model approaches based on the connection of thermal resistances in series or in parallel. Asymptotic solutions focus on the definition of upper (resistances in parallel) and lower bounds (resistances in series). For the unit cell approach, an idealized geometry is the basis for the interconnection of thermal resistances.[17] High effort is required to build up a thermal resistance network, but employing such a model enables to represent diverse unit cell configurations as well as anisotropies. Bracconi et al. and Dubil et al. derived thermal network models that are able to depict diverse anisotropic configurations, the latter being more complex, but versatile and flexible in application.[13,14] A much simpler approach is to modify asymptotic solutions and add estimation parameters.[17] Thus, empirical correlations were established to match experimental data for isotropic cellular materials. For POCS based on the cubic and the tetracaidecahedral—known as "Kelvin"—unit cell, Bianchi et al. set up a model based on numerically derived data.[12] Using the same methodology, Bracconi et al. reestimated and modified the empirical parameters slightly, based on a broader database, including the diamond and the face centered cubic cell.[13] Based on the postulated representative nature of unit cells, the underlying simulations for the models derived were carried out in the Cartesian system, with specified directions of heat conduction. Conclusions from these studies on POCS are that the shape of the strut cross section has little impact on the effective heat conductivity, while the minimum strut diameter is a limiting factor for tapered struts.[12,14] Considering the realization of POCS in the interesting range of a few millimeters regarding strut diameter d_s and cell size l_c, it is reasonable to assume struts with a circular cross section and a constant strut diameter along the strut length, given by additive manufacturing technique. Comparing strut-based POCS with sheet-based periodic structures, such as triply periodic minimal surface structures, the latter exhibit a higher effective heat conductivity, but less permeability for flow applications.[18]

Apart from tackling heat transport problems in terms of heat conduction, POCS promise to adjust the flow field in a favored manner for single- as well as multiphase systems.[3,19–23] Accordingly, POCS are generally used as cylindrical inserts in tube flow applications. Numerical and experimental investigations on the heat transport performance of ceramic, irregular open cell foams in a tube by Razza et al. revealed the extraordinary importance of a solid contact between foam and tube wall.[24] This is ascribed to a high contribution of heat conduction. Busse et al. experimentally corroborated this for POCS. Here, the inner structure and the tube were produced directly as one part by means of additive manufacturing. Step by step, the solid connection between structure and wall ("wall-coupling") was mechanically reduced. Eventually, the comparison between the overall heat transfer coefficient of the resulting POCS with a loose fit to that of the fully wall-coupled structure yields a factor of up to four. Beyond that, the results from the intermediate steps reveal that even a minor extent of wall-coupling causes an intensified heat transfer of more than 2.5 times.[4] However, the technical application of POCS with fixed wall-coupling as catalyst support is restricted. Due to deactivation, the limited lifetime of industrial catalysts (a few years at most) makes a recurrent exchange of POCS inevitable. In contrast, POCS with a loose fit reveal a high wall heat transfer resistance due to a small gap between structure and tube wall.[7,25]

The idea of applying a mechanical function to POCS paved the way toward a novel concept of structured catalyst carriers: Auxetic structures exhibit a negative Poisson's ratio under mechanical load, i.e., they contract perpendicular to a compression load.[26,27] The principle involves designing an auxetic POCS with radial oversize, catalytic coating, compression, and subsequently inserting the POCS into the tubular reactor. If the structure is manufactured from a shape memory alloy,[28,29] the POCS regains its original shape by increasing the temperature. Thus, the wall contact is established by an interference fit in order to intensify the wall heat transfer. Yet, the wall contact is reversible to account for catalyst deactivation and consequently the necessity of a POCS exchange.

Electron beam powder bed fusion (PBF-EB) exhibits a major advantage for the manufacturing of metallic cellular materials. Due to the mechanical stability and the higher heat transport in the sintered powder bed, the building of cellular materials without using supports is easily possible.[30,31] Metallic auxetic lattice structures were successfully fabricated via PBF-EB before.[32–36] The processing of the binary shape memory alloy Nitinol (NiTi) in PBF-EB was recently realized as well.[37–40]

In this contribution, we will present a preselection of auxetic POCS for the possible application in a tube and provide model equations for their geometric and morphological description. Further, we analyze the thermal properties in terms of the effective heat conductivity and provide an adequate model for it as a function of geometric and morphological parameters. Both aspects (geometry and thermal properties) are based on the analysis of the representative elementary volume (REV), according to different auxetic geometries. Once macroscopic POCS are present in a cylindrical shape for the application in a (reactor) tube, we need to discuss the resulting effect on the effective heat

conductivity in radial direction, due to the coordinate transformation. For the analysis of the effective heat conductivity, we apply numerical 3D simulations using COMSOL Multiphysics, in analogy to previous publications on modeling of the effective heat conductivity of conventional POCS.[12,13] In part II of this study, the thermo-mechanical properties of auxetic shape memory POCS are elucidated, exploiting numerical and experimental techniques.[41]

2. Geometry of Auxetic Reentrant POCS

The morphology of isotropic POCS is fully described by two independent geometric parameters, apart from the characteristic unit cell itself. By means of the geometry of the unit cell, cf., Figure 1, model equations can be formulated, which commonly use the strut diameter d_s and the cell size l_c.[3] However, the design of auxetic materials or structures can be more complex, which requires one or more additional parameters. In this work, the focus lies on reentrant structures as they promise the most distinct auxetic effect.[27] In **Figure 2**, the computer-aided designs (CAD) of reentrant structures are depicted. The auxetic effect of these highly anisotropic structures is caused by an inverse honeycomb structure, see Figure 2 (left), while the inversion is described by an eigenmode of the cellular $x-y$-plane with oscillation in z-direction.[27] The extent of inversion can be described by the amplitude $\tilde{A}$ of the curved struts (for a detailed description, see below). In this contribution, the cosine function is used to design the curved struts rather than a simple linear connection between vertical struts, which would result in sharp angles. Thus, the construction provides the advantage of a reduced Poisson's ratio. The dependency of the Poisson's ratio on the struts' morphology is analyzed in part II of this study.[41] Perpendicular to the reentrant plane, layers of cubic or hexagonal cells are possible, cf., Figure 2 (middle, right).

To build the 3D reentrant structure, one single layer "A" is mirrored to form a single stack "AB" that results in the inverse honeycomb. The stack can be repeated vertically as "AB-AB"-stacking to form a structure with squares or hexagons in the cross section, as presented in Figure 2 (right), depicting the potential tube application.[32,34,35] However, by duplicating and shifting the hexagonal cell "B"-layer with subsequent mirroring, a different stacking "AB-CD" is possible, cf., **Figure 3** (top). At last, the hexagonal cell assembly enables the "ABC"-stacking only by duplicating and shifting of the single layer "A," each by l_c, cf., Figure 3 (bottom). The type of stacking influences the free area in the plane of $x-y$-projection, while porosity ε and volume-specific surface area a_v remain the same. Note that the "ABC"-stacking makes larger amplitudes possible, as nodes are opposite to each other across two layers, see Figure 3 (left). This offers an additional degree of freedom in design and mechanical functionality, see part II.[41]

Especially the hexagonal cell reentrant structures are highly anisotropic. The height of the representative unit cell depends on the stacking, and even the base area is a rectangle.[42] Therefore, a uniform unit cell as a cube with equal square faces does not exist. Hence, there is no uniform cell size l_c as depicted in Figure 1. In **Figure 4**, the smallest repeatable units for cubic and hexagonal cell reentrant structures are presented, and in Appendix A1 the characteristic unit cells can be found (Figure A1 and A2). In order to maintain a comprehensible nomenclature and to ensure a systematic construction, the cell size l_c is designated as the edge length of the smallest repeatable unit: a cube for the cubic (Figure 4, top) and a prism with equal edge lengths for the hexagonal cell design (Figure 4, bottom). Thus, the amplitude $\tilde{A}$ is defined in Equation (1):

$$\tilde{A} = a \cdot l_c \tag{1}$$

where a is the dimensionless amplitude factor. Due to the geometry of the cubic cell reentrant structure and the stacking types AB-AB and AB-CD of hexagonal cell design, the theoretical maximum is $a = 0.5$. With respect to the strut diameter and to ensure an auxetic function by compression, $a \leq 0.3$ should be considered. For the hexagonal ABC-stacking, we found $a \leq 0.6$ to be a reasonable choice in order to avoid irreversible mechanical damage due to compression, such as buckling of individual vertical struts or shearing of layers, see part II.[41] From these

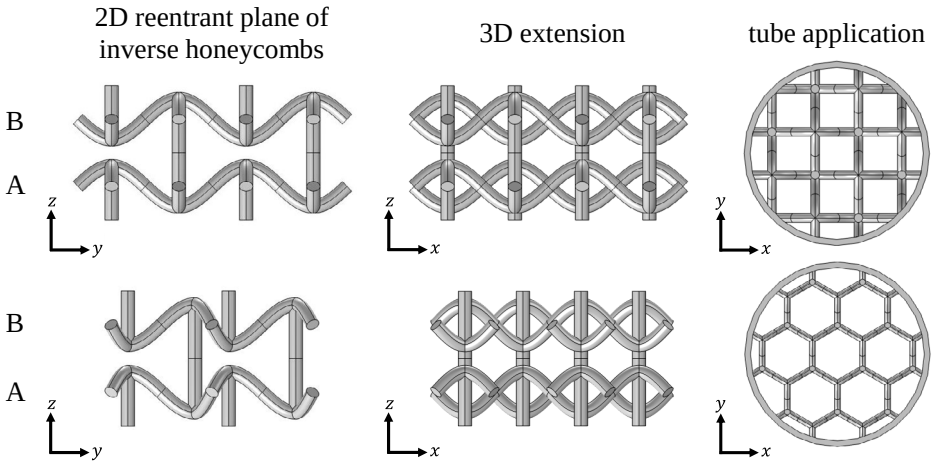

Figure 2. Reentrant plane of inverse honeycombs enabling the auxetic effect (left)[27] for cubic (top) and hexagonal cell structures (bottom), 3D extension by cubic and hexagonal cell layers (middle), and cross sections of a tube application, respectively (right).

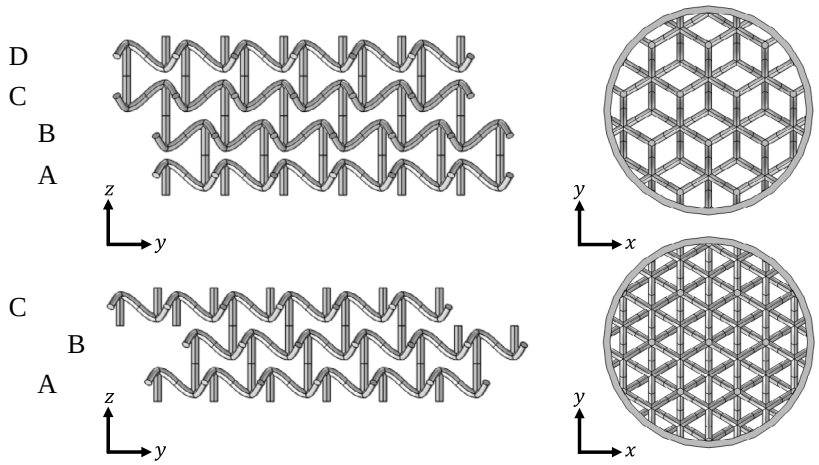

Figure 3. Reentrant plane of inverse honeycombs for different stackings of hexagonal cell reentrant structures (left) and cross sections for a tube application (right).

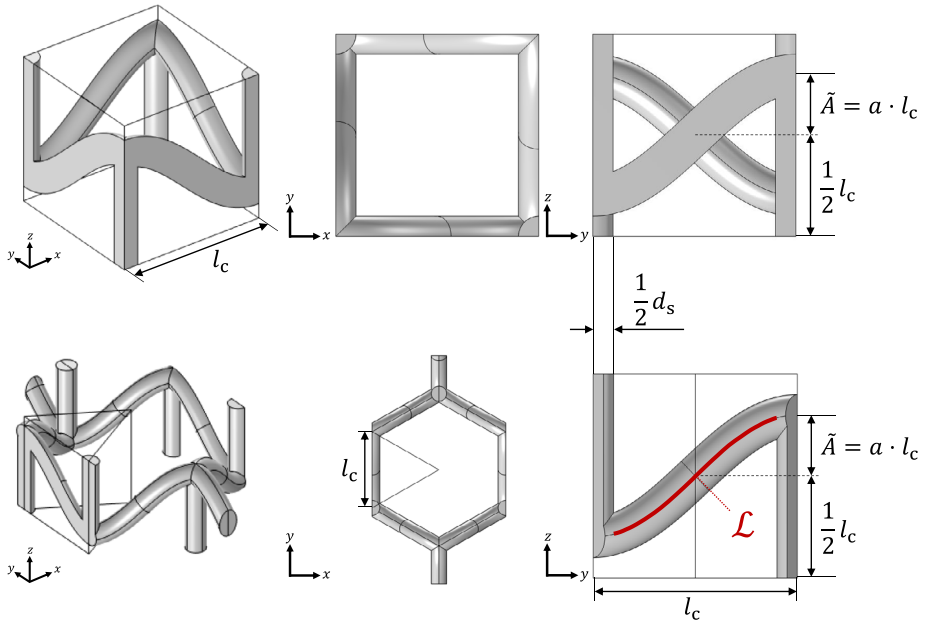

Figure 4. Smallest repeatable units for reentrant structures with cubic cell design, i.e., a cube (top) and with hexagonal cell design, i.e., a prism (bottom). Both units exhibit an amplitude factor of $a = 0.3$ and along with the cell size l_c and the strut diameter d_s a complete description of the geometry is possible.

geometric considerations, it can be stated that the hexagonal cell design of reentrant POCS offers further degrees of freedom regarding mechanical properties, as well as an adjustable porosity and flow behavior in dependence on the stacking (cf., the planar projection of the cross section in Figure 2, 3). In addition, hexagonal cell POCS are more likely to exhibit a good fit in a tube than cubic ones, cf., Figure 2. For these reasons, this contribution focuses, in particular, on the hexagonal cell reentrant POCS, while the cubic cell structures are used for comparison purposes and a broader database.

From the geometry of the smallest repeatable units, cf., Figure 4 (right), the theoretical morphological design equations of porosity ε and volume-specific surface area a_V can be derived, where the latter is related to the total volume of the unit. For this, further definitions and characteristic entities are required. The characteristic ratio ϕ of l_c and d_s is defined in Equation (2) as:

$$\phi = \frac{l_c}{d_s} \tag{2}$$

The length of the curved strut $\mathcal{L}$ (see Figure 4) is defined for both structure types in Equation (3) as:

$$\mathcal{L} = \int_{d_s/2}^{l_c - d_s/2} \sqrt{1 + (a \cdot \pi)^2 \sin^2\left(\pi \frac{x}{l_c}\right)}\, \mathrm{d}x \tag{3}$$

For a clear presentation, the auxiliary parameter B will be used for the respective structure:

$$B_{\mathrm{cub}} = \frac{2}{d_s}\left(\tilde{A} + 2\mathcal{L}\right) \text{ and}$$

$$B_{\mathrm{hex}} = \frac{1}{d_s}\left(2\tilde{A} + 3\mathcal{L}\right)$$

The resulting correlations for the porosity and the volume-specific surface area are given in Equation (4)–(7):

$$\varepsilon_{\mathrm{cub}} = 1 - \frac{\pi(\phi + B_{\mathrm{cub}}) + 4 \cdot \left(\pi - \left(\sqrt{2} + \frac{2}{3}\right)\right)}{8\phi^3} \tag{4}$$

$$a_{\mathrm{V,cub}} = \frac{\pi(\phi + B_{\mathrm{cub}}) + 4 \cdot \left(\pi - \left(\frac{3}{2}\sqrt{2} + 1\right)\right)}{2\phi^2 \cdot l_c} \tag{5}$$

$$\varepsilon_{\mathrm{hex}} = 1 - \frac{\sqrt{3}\pi(\phi + B_{\mathrm{hex}}) + \sqrt{3} \cdot 3\pi - 9}{18\phi^3} \tag{6}$$

$$a_{\mathrm{V,hex}} = \frac{2\sqrt{3}\pi(\phi + B_{\mathrm{hex}}) + \sqrt{3} \cdot 6\pi - 27}{9\phi^2 \cdot l_c} \tag{7}$$

To the authors' knowledge, these design equations for such auxetic structures have not been reported before. Porosity and volume-specific surface area represent important morphological parameters in process engineering and the design of chemical reactors. The detailed steps of the derivation can be found in Appendix A2. To establish such accurate correlations, it is necessary to separately consider the respective node. Yet, for the nodes, the correlations do not take into account the curvature of the struts (cf., Appendix A2). Therefore, for high amplitude factors a and low ϕ there will be slight deviations from the correct values. For example, for $\phi = 3$ the absolute maximum deviations of porosity are in the range of 0.4% for cubic and 0.27% for hexagonal cell structures, whereas for $\phi = 5$ the deviations are only 0.06% for both structure types. In **Figure 5**, the porosity correlations of cubic and hexagonal reentrant structures are depicted as a function of ϕ. Further, porosity decreases with a, but to maintain a void between two opposite nodes the condition is $a < 0.5(1 - \phi^{-1})$ for ABAB-stacking (cf., Figure 2 and 4). Hence, with higher amplitude factors a, ϕ must be higher. For ABC-stacking, the condition is $a < 0.5(2 - \phi^{-1})$. Moreover, cubic cell structures possess a higher solid fraction for the same ϕ, resulting in higher slopes in Figure 5. Therefore, the same change, e.g., in d_s with constant l_c, shows a stronger influence on the porosity of the cubic than the hexagonal cell reentrant structures.

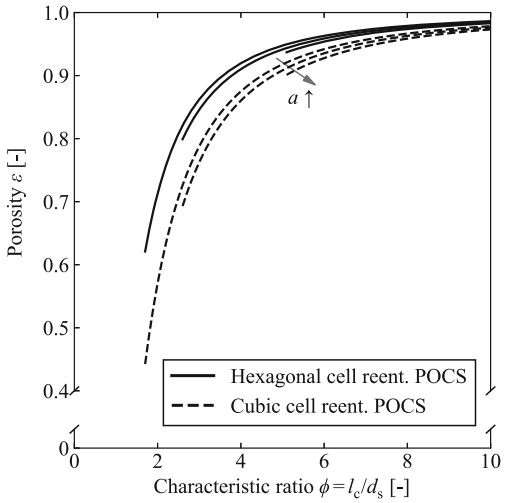

Figure 5. Porosity correlations of cubic and hexagonal cell reentrant structures with amplitude factors $a = \{0.2, 0.3, 0.4\}$ and ABAB-stacking as the limiting condition for the characteristic ratio ϕ.

3. Methods and Models

The applied tool for simulation, COMSOL Multiphysics (version 6.1), differs considerably in the numerical approach from OpenFOAM that was used in previous fundamental studies on thermal conductivity of POCS.[12–14] OpenFOAM is based on the finite volume method, whereas COMSOL Multiphysics employs the boundary element method. This method is complementary to the finite element method,[43] which makes this software very suitable for the simulation of heat conduction, as temperature values are set equal at the boundaries of neighboring elements. In these simulations, the Laplace equation of stationary heat conduction is solved.[12,13] However, to our knowledge only few contributions dealing with sole heat conduction in cellular materials use this simulation toolbox and information regarding numerical approaches and quality control are scarce.[16,44,45] Therefore, we present a mesh and discretization analysis along with the description of numerical methods that are selected in the software toolbox for stationary heat transfer studies, see Appendix A3.[43,46] Furthermore, comparative simulations were carried out with isotropic cubic and Kelvin unit cells for validation with the literature data, see Section 3.1.[12,13] For this purpose, the isotropic unit cells depicted in Figure 1 are used for simulation. For the cubic and hexagonal cell reentrant structures investigated in this study, the particular REVs are shown in **Figure 6**. The REV of the cubic cell reentrant structure is identical to its smallest repeatable unit; the REV of the hexagonal cell reentrant structure consists of six of its smallest repeatable units from Figure 4. All structures investigated were designed using the built-in CAD tool of the software. Particular care was taken during the design process in order to eliminate any possible overlapping spaces of single struts, as these may affect simulation results.

The variations in geometry parameters are listed in **Table 1** and with respect to the strut diameter, down to a general manufacturing limit of $d_s = 0.2$ mm.[3,20] By this, a comprehensive database is established for the development of a universal model for the effective heat conductivity of reentrant POCS. The chosen solid material from the COMSOL database is Titanium beta-21S for all simulations (material heat conductivity $k_{\mathrm{Ti}} = 7.5\ \mathrm{Wm^{-1}K^{-1}}$).[43]

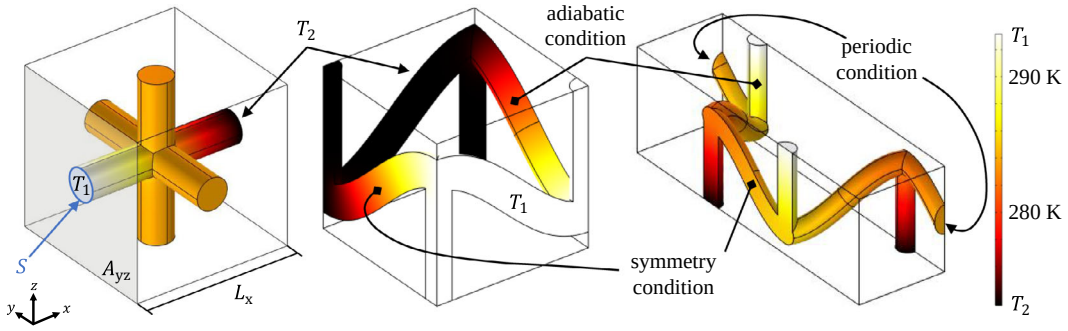

Figure 6. The REVs for heat conduction including the graphically illustrated simulation results: isotropic cubic unit cell with heat conduction in *x*-direction (left), REV of cubic cell reentrant structure with heat conduction in *y*-direction (middle), and REV of hexagonal cell reentrant structure with heat conduction in *z*-direction (right). For the REVs shown, the geometry parameters are set to $\phi = 5$, and $a = 0.3$ where it applies. The boundary conditions are marked exemplary. Isothermal cut surface area S and area A_{yz} according to Equation (8) and (9).

Table 1. Investigated variations in geometry parameters of reentrant structures.

Reentrant structure	Cell size l_c [mm]	Strut diameter d_s [mm]	Amplitude factor a [−]
Cubic cell	{3, 4, 5}	0.2–1.4 (0.2 steps)	0.0–0.5 (0.1 steps)
Hexagonal cell	{3, 4, 5}	0.2–1.5 (0.1 steps)	0.0–0.8 (0.1 steps)

In addition to the REVs for heat conduction, Figure 6 shows the boundary conditions applied in the simulations. The surfaces of struts are adiabatic, i.e., thermally insulated. For most of the cut surfaces, it is reasonable to apply symmetry boundary conditions (equivalent to thermal insulation). However, for the hexagonal structure, a periodic condition in *y*-direction is necessary. Finally, two faces opposite to each other are set to specific temperatures, namely, $T_1 = 293.15$ K and $T_2 = 273.15$ K, in order to simulate conductive heat flow along a fixed temperature difference ΔT of 20 K. The initial value of the domain was set to 273.15 K, as was the reference temperature for the simulation.

For numerical simulations, the mesh resolution and element size are crucial. The utilized software offers a preset of different mesh settings and element size categories, see Table A2 in Appendix A3. By discretization using base functions, a single mesh element is divided into a certain amount of intervals depending on the order of the base functions, and the respective value of the balanced entity is approximated by the set of base functions (interpolation). The combination of element size and order of discretization yields the resolution that the final equation system provides. To avoid an ill-conditioned system, a preliminary analysis is required. In fact, divergence in simulation results may arise from an excessively high resolution due to round-off errors, in particular for high orders of base functions.[43,46] According to the mesh and discretization analysis in Appendix A3, for all simulations presented in this contribution the element size category 3 is chosen along with the shape function "quartic Lagrange." For the approximation of the solution of differential equations, COMSOL Multiphysics employs the Galerkin method.[43] In order to solve the resulting linear equation system, the direct Panua-PARDISO solver is applied in this work.[47] All other settings are retained as default.

As result of the simulations, the conductive heat flux q normal to the respective isothermal face with the cut surface area S (see Figure 6) is integrated and the resulting heat flow Q is determined in Equation (8):

$$Q = \iint_S q \, \mathrm{d}S \tag{8}$$

Resulting from the approach of heat conduction by Fourier, Equation (9)

$$k_{\mathrm{eff,x}} = \frac{L_\mathrm{x} \cdot Q}{A_{yz} \cdot \Delta T} \tag{9}$$

computes the effective heat conductivity $k_{\mathrm{eff,x}}$ in *x*-direction using L_x as distance between the two isothermal faces and A_{yz} as the overall area of the unit's side face perpendicular to the direction of heat conduction, see Figure 6.[12] In the cases of isotropic unit cells, the effective conductivity coefficients are equal in every spatial direction, i.e., $k_{\mathrm{eff,x}} = k_{\mathrm{eff,y}} = k_{\mathrm{eff,z}} = k_{\mathrm{eff}}$.[12] The effective heat conductivity of the cubic cell reentrant structure is equal in *x*- as well as *y*-direction, cf., Figure 6. Hence, a single simulation is sufficient. For the hexagonal cell reentrant structure, every single spatial direction is considered separately. In order to characterize the effective heat conductivity k_{eff} in dependence on geometry parameters and to compare the results with the literature data, the derived values are normalized with the corresponding material property to give the dimensionless effective heat conductivity $\hat{k}_{\mathrm{eff}}$, see Equation (10):

$$\hat{k}_{\mathrm{eff}} = \frac{k_{\mathrm{eff}}}{k_{\mathrm{Ti}}} \tag{10}$$

3.1. Literature Correlations and Method Validation

In this work, we consider the general correlation in Equation (11) that describes $\hat{k}_{\mathrm{eff}}$ as a function of the morphological parameters solid fraction, namely, $(1 - \varepsilon)$, and tortuosity τ:

$$\hat{k}_{\text{eff}} = \frac{1-\varepsilon}{\tau} \tag{11}$$

Several empirical expressions for τ exist, mainly representing functions of porosity or solid fraction with respect to the phase applied (fluid or solid). In the case of effective heat conduction in POCS, the solid phase is the one of interest. The derived empirical correlations for tortuosity τ are given by Bianchi et al. as in Equation (12) and by Bracconi et al. as in Equation (13):[12,13]

$$\text{Bianchi et al. (2016):} \quad \tau = [0.36 + 0.64(1-\varepsilon)]^{-1} \tag{12}$$

$$\text{Bracconi et al. (2020):} \quad \tau = \left[\frac{1}{3} + \frac{2}{3}(1-\varepsilon)\right]^{-1} \tag{13}$$

Originating from an asymptotic approach, these correlations are based on the general formula of τ in Equation (14):

$$\tau = [\alpha + (1-\alpha)(1-\varepsilon)]^{-1} \tag{14}$$

where α is the empirical parameter. For a solid fraction of 1 ($\varepsilon = 0$), this formula yields the heat conductivity of the solid material, i.e., $\hat{k}_{\text{eff}} = 1$.

The herein presented settings for simulation are validated by comparing results from simulations of the isotropic cubic and Kelvin unit cells with the literature correlations that Bianchi et al. and Bracconi et al. derived.[12,13] For the cubic unit cell, the geometry parameters from mesh analysis are used, see Table A1 in Appendix A3; parameter settings of the Kelvin unit cell are listed in **Table 2**. The CAD models of the Kelvin unit cell with the respective parameter combinations were imported as STL files.

In **Figure 7**, the derived data of $\hat{k}_{\text{eff}}$ are plotted versus the solid fraction of the structures. Most of the data lie in between the two curves, further deviations are in the range of +1% for Bianchi et al. and −3% for Bracconi et al. The presented data in Figure 7 show very good agreement to the literature correlations, even in an extrapolated range up to a solid fraction of 0.4. Based on these results and the mesh and discretization analysis in Appendix A3, we assess the herein presented methods and settings for COMSOL Multiphysics to be adequate for simulations of heat conduction in reentrant POCS.

3.2. Numerical Setup for the Investigation on the Effective Radial Heat Conductivity

Since the objective is the application of auxetic POCS in tubular reactors, we further investigate the effective radial heat conductivity $\hat{k}_{\text{eff,r}}$ of POCS. The computation domain is a disc of cells with one layer height that is further diminished to a cutout

Table 2. Geometry parameter settings of the Kelvin unit cell for validation with literature correlations.

Structure	Cell size l_c [mm]	Strut diameter d_s [mm]	Characteristic ratio ϕ [−]
Isotropic Kelvin	3	{0.5, 0.8}	{6, 3.75}
	5	{0.5, 1.0, 1.5}	{10, 5, 3.$\overline{3}$}

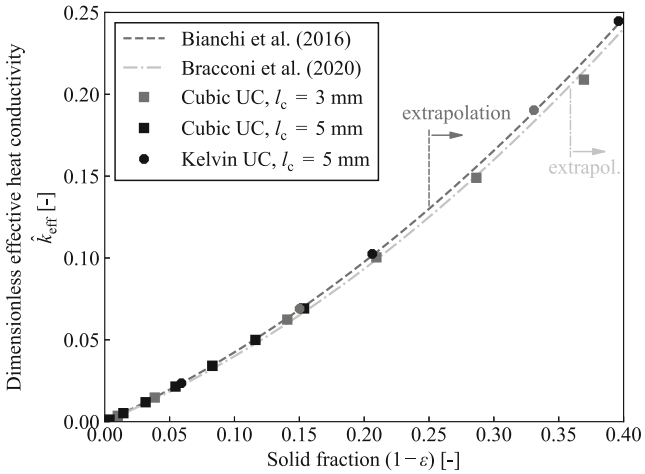

Figure 7. Validation of the applied numerical approach by comparing simulation results of isotropic unit cells with literature correlations by Bianchi et al. and Bracconi et al.[12,13]

subdomain. In the case of cubic cells, the cutout is a wedge of 90°; for the hexagonal cell, it is 120°. The cut surfaces are set to symmetry boundary condition. The basic design considers a vertical strut in the center, i.e., the tube axis, and a constant $l_c = 5$ mm. The investigations on isotropic cubic unit cell POCS serve as reference to which both reentrant structures are compared at equal solid fractions and $a = 0.0$. For this, the strut diameters are adjusted by means of Equation (4) and (6), and for the isotropic unit cell the correlation for porosity by Klumpp et al. was used.[48] Furthermore, the inner tube diameter D_t is varied and thus the number of cells per tube diameter (CPD_t), which is the ratio $D_t l_c^{-1}$. For the hexagonal cell structure, an additional factor of $\left(\sqrt{3}\right)^{-1}$ must be applied on CPD_t, as the width of the unit cell is $\sqrt{3}l_c$ (see Appendix A1). Moreover, the influence of the amplitude of the curved struts on the effective radial heat conductivity is investigated. All geometry parameters applied are listed in **Table 3**.

For a proper analysis of $\hat{k}_{\text{eff,r}}$, the area of the face A_{xy} in Equation (9) has to be chosen correctly in order to adapt to polar coordinates. The mean surface area A_m of a hollow cylinder is calculated by Equation (15):

$$A_m = 2\pi H \frac{r_o - r_i}{\ln\left(\frac{r_o}{r_i}\right)} \tag{15}$$

where H is the height of the cylinder, r_o is the outer radius, and r_i is the inner radius. Therefore, the POCS' vertical strut in the center of the tube is cut out, leaving an inner radius of $r_i = 0.5 \cdot d_s$ of the POCS wedge. Hence, the outer radius r_o of the cylindrical POCS corresponds to the respective (inner) tube diameter D_t. **Figure 8** shows exemplary the computation domains. $T_1 = 293.15$ K is applied in the center of the representative POCS disc. The resulting effective radial heat conductivity is determined via Equation (16):

Table 3. Variations in geometry parameters for investigating the effective radial heat conductivity. Cell size is constant with $l_c = 5$ mm.

Structure	Cells per tube diameter $CPD_t = D_t l_c^{-1}$ [–]	Strut diameter d_s [mm]	Amplitude factor a [–]	Solid fraction[a] $(1-\varepsilon)$ [–]
Isotropic, cubic cell	1–39	1		0.0829
Reentrant, cubic cell	1–39	1.0928	0.0	0.0829
	1–39		0.2	0.0972
	1–37		0.4	0.1215
Reentrant, hexagonal cell[b]	0.6–34	1.392	0.0	0.0829
	0.6–34		0.2	0.0986
	0.6–27		0.4	0.1233
	0.6–17		0.6	0.1526

[a]w.r.t.[48] for isotropic cubic unit cell POCS, and Equation (4) and (6) for reentrant structures. [b]$CPD_t = D_t(\sqrt{3}\cdot l_c)^{-1}$.

$$\hat{k}_{\text{eff,r}} = \frac{\ln\left(\frac{r_o}{r_i}\right) Q}{\frac{2\pi}{f} H k_{\text{Ti}} \Delta T} \tag{16}$$

with f representing the factor of the cutout fraction (4 for 90° and 3 for 120°), and $H = l_c$, as the POCS disc is built of one cell layer. Equation (8) still prevails to calculate Q, but now for a curved cut surface area S. For these simulations, the heat flow both at the center and at the outer cut surface is determined in order to check on consistency. The mean value is used for analysis.

Note that all simulations presented in this article are based on the assumption of isotropic material properties. Any mechanical stress induced by temperature gradients or compression load is neglected. Thus, the focus lies solely on the effective heat conductivity as a function of geometric and morphological parameters. A discussion of the coupled thermal stress analysis would require the consideration of many effects, which makes the corresponding simulation very complex. In reality, the manufactured shape memory POCS are expected to possess highly anisotropic material properties. The texture of NiTi is determined by the build direction in the PBF-EB process, which greatly affects the mechanical properties of parts with different spatial orientations.[30,49] A consequence of this will be an anisotropic and complex stress state within the struts. In addition, a temperature as well as a stress-induced phase transition of NiTi would have to be considered.[39,49] Suitable models only exist to a limited extent for this. A deeper understanding of shape memory alloy processes along with detailed models will enable rigorous simulations in the future.

4. Results and Discussion

In the following, the results on the effective heat conductivity $\hat{k}_{\text{eff}}$, obtained from simulations of the REVs with a specified direction of heat conduction in the Cartesian system (see Figure 6), are presented and discussed. Subsequently, these results are processed to develop a more specific empirical correlation for the effective heat conductivity of reentrant structures in analogy to Equation (11) and (14). It provides the basis for ongoing and future studies, and for the design of diverse applications utilizing reentrant POCS. Finally, the findings of the spatially resolved investigation on the effective radial heat conductivity $\hat{k}_{\text{eff,r}}$ are presented and consolidated to an empirical correlation.

4.1. Characterization of Effective Heat Conductivity

For the hexagonal cell structure, the dimensionless effective heat conductivities $\hat{k}_{\text{eff,x}}$ in x- and $\hat{k}_{\text{eff,y}}$ in y-direction obtained from simulations are exemplary presented and plotted against the solid fraction for two cell sizes l_c in **Figure 9**. The results for the reentrant cubic cell design can be found in **Figure 10**. In general, with a higher solid fraction, i.e., larger d_s with constant l_c, $\hat{k}_{\text{eff}}$ increases, as expected from previous studies.[12–14] However, with increased amplitude factors a of the curved struts, $\hat{k}_{\text{eff}}$ decreases, except for heat conduction in y-direction in the hexagonal cell REV with the lowest ϕ.

For all other parameter combinations and both cell types, we find for a fixed strut diameter d_s (or fixed ϕ, respectively) that with every increment the amplitude factor a increases, the solid fraction increases correspondingly (cf., Figure 5) and $\hat{k}_{\text{eff}}$ decreases. Although with lower values of ϕ the effect of a diminishes in x- and y-direction, see Figure 9 and 10, it remains unchanged in z-direction, see Figure 10 (right).

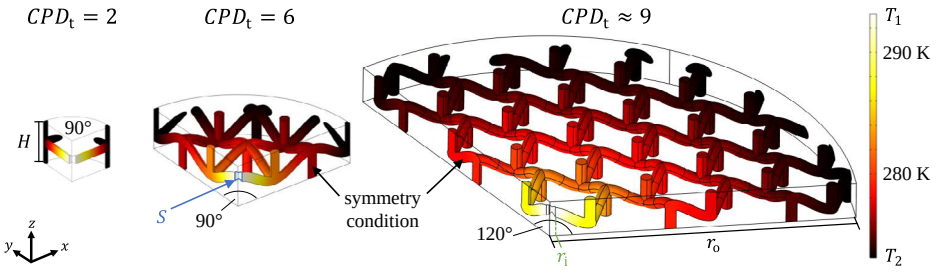

Figure 8. Exemplary computation domains used for numerical evaluation of the effective radial heat conductivity $\hat{k}_{\text{eff,r}}$ of POCS, including the graphically illustrated simulation results: cutout discs of isotropic unit cell POCS with $CPD_t = 2$ (left), cubic cell reentrant POCS with $CPD_t = 6$ (middle), and hexagonal cell reentrant POCS with $CPD_t \approx 9$ (right); $a = 0.2$.

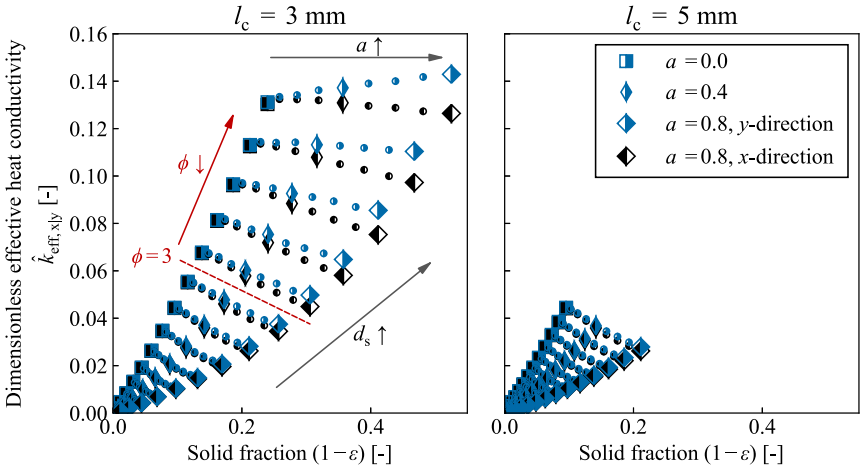

Figure 9. Dimensionless effective heat conductivity $\hat{k}_{eff}$ of hexagonal cell reentrant POCS in x- and y-direction (cf., Figure 6) in dependence on solid fraction and amplitude factor a, for $l_c = 3$ mm (left) and $l_c = 5$ mm (right). The circles • are displaying $\hat{k}_{eff}$-values for intermediate amplitude factors a. The legend applies to both diagrams.

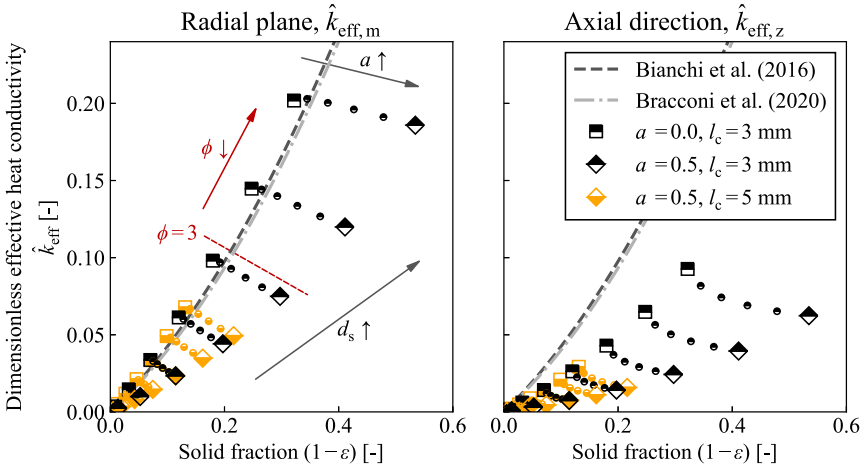

Figure 10. Effective heat conductivity in dimensionless form in the radial plane $\hat{k}_{eff,m}$ (cf., Equation (17); left), and dimensionless effective heat conductivity in z-direction $\hat{k}_{eff,z}$ (right) of cubic cell reentrant POCS, respectively, in dependence on solid fraction and amplitude factor a. Comparison with literature correlations as reported.[12,13] Legend applies to both diagrams; the circles • are displaying $\hat{k}_{eff}$-values for intermediate amplitude factors a.

Due to the anisotropy of the reentrant POCS and in accordance with the application in tubes, two domains are focused on in the following: the vertical or axial domain, according to a tube axis, i.e., the z-direction, and the horizontal or radial plane, for which the mean average of $\hat{k}_{eff,x}$ and $\hat{k}_{eff,y}$ is calculated by Equation (17):

$$\hat{k}_{eff,m} = \frac{1}{2}\left(\hat{k}_{eff,x} + \hat{k}_{eff,y}\right) \tag{17}$$

Note that the averaged $\hat{k}_{eff,m}$ represents the dimensionless effective heat conductivity in the radial plane, but is based on the simulations of heat conduction in the REV, i.e., in the Cartesian system. Equation (17) applies to hexagonal and cubic cell reentrant POCS, but for the latter $\hat{k}_{eff,x}$ and $\hat{k}_{eff,y}$ are identical.

For hexagonal cell structures, the simplification regarding Equation (17) is appropriate, considering the simulation results depicted in Figure 9 (left). For $\phi \geq 3$, the values are almost identical with slight deviations for high a. Since values for $\phi < 3$ significantly deviate for x- and y-direction, these will be neglected in the following. This is justified because for low ϕ only few geometry parameter combinations are feasible (see Figure 5) and the auxetic effect diminishes for such low porosities, see part II.[41] In general, pronounced auxetic structures exhibit a high porosity.[36,50]

Another fact clearly seen when comparing the data in Figure 9 and 10, respectively, is that for specific POCS unit cells with the same characteristic ratio ϕ and the same a, $\hat{k}_{eff}$ is identical. This underlines the direct dependency of the effective heat conductivity on solid fraction since solid fraction and characteristic ratio ϕ are directly coupled, cf., Section 2 and Equation (4) and (6). Note

that this holds for the assumption of struts with a constant cross section.

In **Figure 11** (left), $\hat{k}_{\mathrm{eff,m}}$ is plotted for the hexagonal cell reentrant POCS with $l_c = 5$ mm and compared to the literature correlations.[12,13] Interestingly, for the amplitude factor $a = 0.0$ the effective heat conductivity exceeds the literature correlations, whereas data for $a = 0.1$ show a very good agreement.[12,13] This is in line with the results for the cubic cell design in Figure 10, left. Since the parameter settings with low a do not represent a pronounced auxetic behavior, see part II,[41] these results can be explained considering the rather uniform design of the (almost) straight struts.

In Figure 10 and 11, right, the anisotropic character of reentrant POCS is clearly recognizable. In axial direction, the heat flux is severely hindered by the reentrant geometry in general, i.e., the inverse honeycomb cell design, see Section 2. This results in the distinct deviation from the literature correlations. Higher values of a amplify this additionally. However, with a constant amplitude factor a the course of $\hat{k}_{\mathrm{eff,z}}$ over the solid fraction still shows a parabolic behavior, which is the basic mathematical function described by Equation (11) and (14). Overall, cubic cell reentrant POCS reveal a slightly higher effective heat conductivity than the hexagonal ones at similar solid fractions.

The explanation for the presented interrelations lies in the tortuous path of heat conduction in the POCS' smallest repeatable unit, see Figure 4. For a larger amplitude, there is a longer distance for heat conduction in any direction, and thus, the effective heat conductivity is decreased. This lengthened transport distance can be described most adequately by the tortuosity τ, corresponding to the length of the curved strut $\mathcal{L}$ in relation to the effective width of the unit, i.e., $(l_c - d_s)$. Hence, by following Equation (11) and (14), we propose an extended correlation for the tortuosity to apply on reentrant structures in Equation (18):

$$\tau = \left(\frac{\mathcal{L}}{l_c - d_s}\right)^{\beta} \cdot [\alpha + (1-\alpha)(1-\varepsilon)]^{-1} \tag{18}$$

The coefficients α and β represent empirical parameters. The adequacy of Equation (18) is evaluated in the following section.

4.2. Empirical Model for Reentrant POCS Based on the REV

In order to confirm the approach of Equation (18), we eliminate the influence of the extended tortuosity, originating from the curved struts, on the effective heat conductivity in the graphical representation as described below. **Figure 12** shows the averaged simulation results $\hat{k}_{\mathrm{eff,m}}$ in the radial plane for hexagonal cell reentrant POCS with $l_c = \{3, 5\}$ mm and $\phi \geq 3$ plotted versus a modified solid fraction that is described in the following Equation (19) and (20):

$$\text{modified solid fraction: } \frac{(1-\varepsilon)}{\tau^*} \tag{19}$$

$$\text{with } \tau^* = \left(\frac{\mathcal{L}}{l_c - d_s}\right)^{\beta} \tag{20}$$

and $\beta = 1.5$. Note that the factor of additional tortuosity τ^* is 1 for $a = 0.0$. The literature correlations are still plotted versus the regular solid fraction $(1-\varepsilon)$ (i.e., $\beta = 0$). This results in two abscissae in Figure 12 for comparative purposes. Using this graphical representation, a reasonable comparison is possible and the simulation results show a good agreement with the literature correlations. Consequently, it is appropriate to describe the basic course of $\hat{k}_{\mathrm{eff}}$ with the existing approach of previous publications using solid fraction and tortuosity (cf., Equation (11) and (14)) and to describe the additional influence on tortuosity

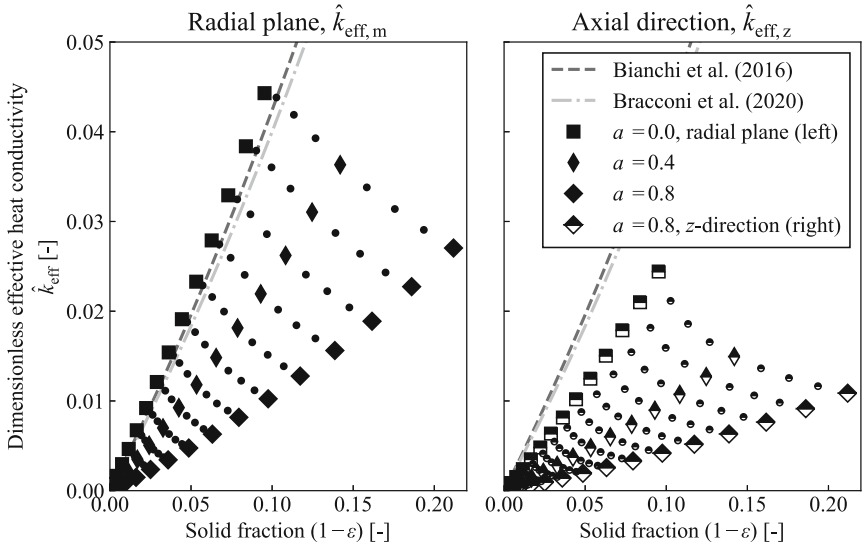

Figure 11. Averaged effective heat conductivity in dimensionless form in the radial plane $\hat{k}_{\mathrm{eff,m}}$ (cf., Equation (17); left), and dimensionless effective heat conductivity in z-direction $\hat{k}_{\mathrm{eff,z}}$ (right) of hexagonal cell reentrant POCS with $l_c = 5$ mm, respectively, in dependence on solid fraction and amplitude factor a. Comparison with the literature correlations as reported.[12,13] The legend applies to both diagrams; the circles • are displaying $\hat{k}_{\mathrm{eff}}$-values for intermediate amplitude factors a.

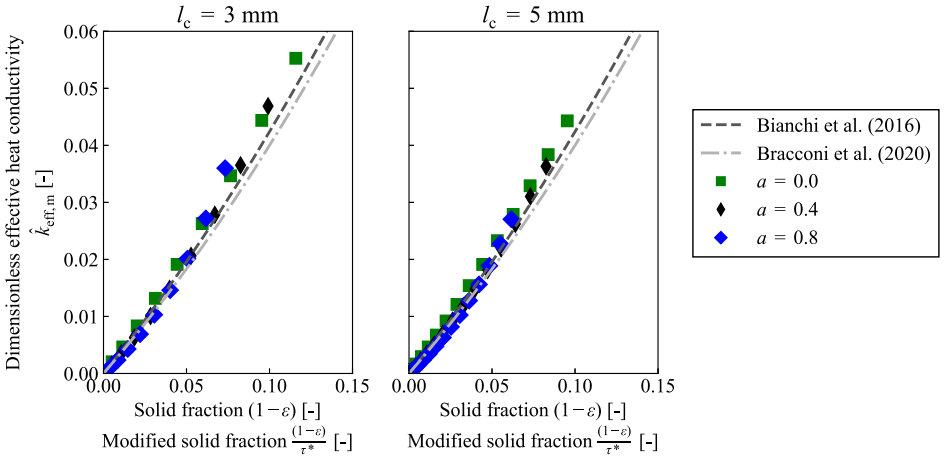

Figure 12. Averaged effective heat conductivity in dimensionless form in the radial plane $\hat{k}_{eff,m}$ of hexagonal cell reentrant POCS in dependence on the modified solid fraction (cf., Equation (19) and (20)) with $\beta = 1.5$, for $l_c = 3$ mm (left) and $l_c = 5$ mm (right). Two abscissae are used to compare data with reported literature correlations.[12,13]

originating from the auxetic design with the extension given in Equation (18).

We applied the least squares method for parameter estimation, using the python module SciPy.optimize to minimize the normalized squared error. This included the dataset of $l_c = \{3, 5\}$ mm, whereas data of $l_c = 4$ mm served as independent data for validation. As a qualitative measure, we provide the mean absolute percentage error (MAPE) between the correlation, which is based on Equation (11) and (18), and simulation results.

In a preliminary analysis, we used the proposed correlation in Equation (18) with $\alpha = 1/3$ (cf., Bracconi et al.[13]), and only $\beta = 1.69$ was fitted to match the simulation results. For the hexagonal cell reentrant POCS, a pronounced drift and underestimation was observed for lower ϕ (MAPE of 7.6% for $\hat{k}_{eff,m}$). Therefore, α has been adjusted as described below.

General correlations were set up using all simulation data available with $\phi \geq 3$ for both domains (radial plane and axial direction) and for both reentrant structures, respectively. Using the derived model equations for porosity (Equation (4) and (6)), the model datasets of dimensionless effective heat conductivity $\hat{k}_{eff}$ are calculated via Equation (11) and (18). The following results of the parameter estimation are given in **Table 4**, where the MAPE corresponds to the independent dataset with $l_c = 4$ mm. Moreover, we differentiate between the assessment in the total geometrical parameter range and in a narrowed range of interest, including limitations in additive manufacturing via PBF-EB. The main limiting factor of PBF-EB is given by the resolution, i.e., the minimal strut diameter d_s. To account for the mechanical functionality and a proper auxetic behavior, further limits are set, see part II.[41] The narrowed range corresponds to geometry parameters given in **Table 5**.

Table 4 provides the empirical parameters to compute the effective heat conductivity $\hat{k}_{eff}$ based on the solid fraction $(1-\varepsilon)$ and tortuosity τ, see Equation (11) and (18), along with Equation (4) and (6). According to the given deviations in Table 4, the model is considerably accurate, especially for the radial plane domain. For hexagonal cell reentrant POCS (model $H_{x|y,m}$), Figure A8 in Appendix A4 shows the parity plot with an error band of ±15% for all geometry parameter combinations with $\phi \geq 3$. However, a slight systematic drift is recognizable, probably because low values of ϕ diminish the effect of a on $\hat{k}_{eff,m}$. In the range of higher $\hat{k}_{eff,m}$ values, which corresponds to the narrowed range of interest as for the application in catalytic reactors, effective heat conductivity is underestimated by the general model. **Figure 13** shows this quite clearly, where the filled

Table 4. Results of parameter estimation with empirical parameters α and β corresponding to Equation (18), yielding the tortuosity.

Reentrant structure	Domain	Empirical parameters		MAPE[a,b] [%]	MAPE[a,c] [%]	Model abbreviation
		α [−]	β [−]			
Cubic	Radial plane	0.41	1.93	3.31	2.95	$C_{x\|y,m}$
	Axial direction z	0.13	3.08	12.95	15.97	C_z
Hexagonal	Radial plane	0.37	1.85	5.67	4.94	$H_{x\|y,m}$
	Axial direction z	0.16	2.32	7.35	10.18	H_z

[a)]MAPE with respect to the independent data with $l_c = 4$ mm. [b)]MAPE for the total parameter range. [c)]MAPE for the narrowed range of interest in geometry parameters, see Table 5.

Table 5. Narrowed range of interest of geometric parameters including limitations in additive manufacturing via PBF-EB.

Reentrant structure	Characteristic ratio ϕ [−]	Strut diameter d_s [mm]	Amplitude factor a [−]
Cubic	3–6.25	0.8–0.12	0.2–0.4
Hexagonal			0.2–0.6

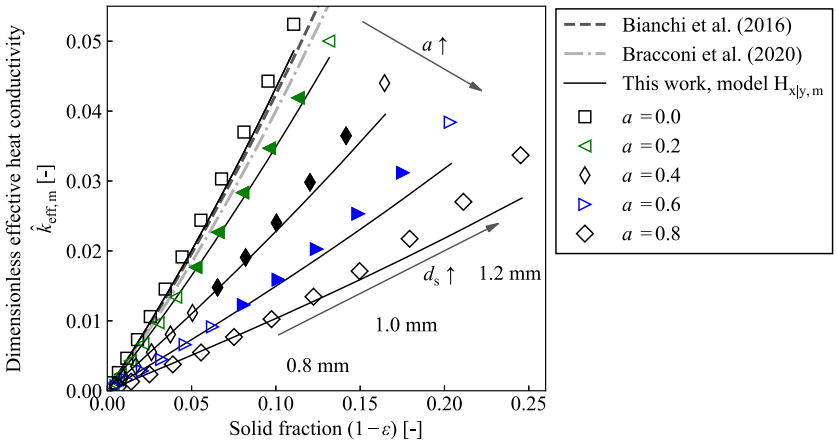

Figure 13. Averaged effective heat conductivity in dimensionless form in the radial plane $\hat{k}_{\mathrm{eff,m}}$ for the hexagonal cell reentrant structure. Results obtained by simulations using $l_c = 4$ mm as independent data are indicated as markers. Filled markers represent data within the narrowed range of interest, cf., Table 5. Curves represent the model correlation $H_{x|y,m}$ developed within this work and the literature correlations as reported.[12,13]

markers indicate the narrowed range of interest. For amplitude factors below 0.4, the model fit is accurate. In contrast, model H_z for the axial domain overestimates the effective heat conductivity $\hat{k}_{\mathrm{eff,z}}$; the respective plots can be found in Appendix A4. The models presented here can be used for an overall description of the effective heat conductivity of cubic and hexagonal cell reentrant structures, regardless of the absolute dimensions of the geometric parameters. However, the model is only valid for the characteristic ratio $\phi > 3$ and amplitude factors $a \leq 0.5$ and $a \leq 0.8$ for cubic and hexagonal cell designs, respectively.

In order to account for the systematic deviation in the presented model (Figure A8), a reparameterization is done for the narrowed range of interest of geometric parameters. The results can be found in Appendix A4. The derived models $C_{x|y,m}$* and $H_{x|y,m}$* exhibit an increased accuracy, i.e., a MAPE of 1.64% and 2.79%, respectively, and will be used in the following.

4.3. Effective Radial Heat Conductivity

The investigations on the effective radial heat conductivity of cubic and hexagonal cell reentrant POCS reveal a considerable change of $\hat{k}_{\mathrm{eff,r}}$ with the number of cells per tube diameter (CPD_t), see **Figure 14**. The isotropic cubic unit cell POCS serve as reference. Heat fluxes at the center and at the outer cut surface

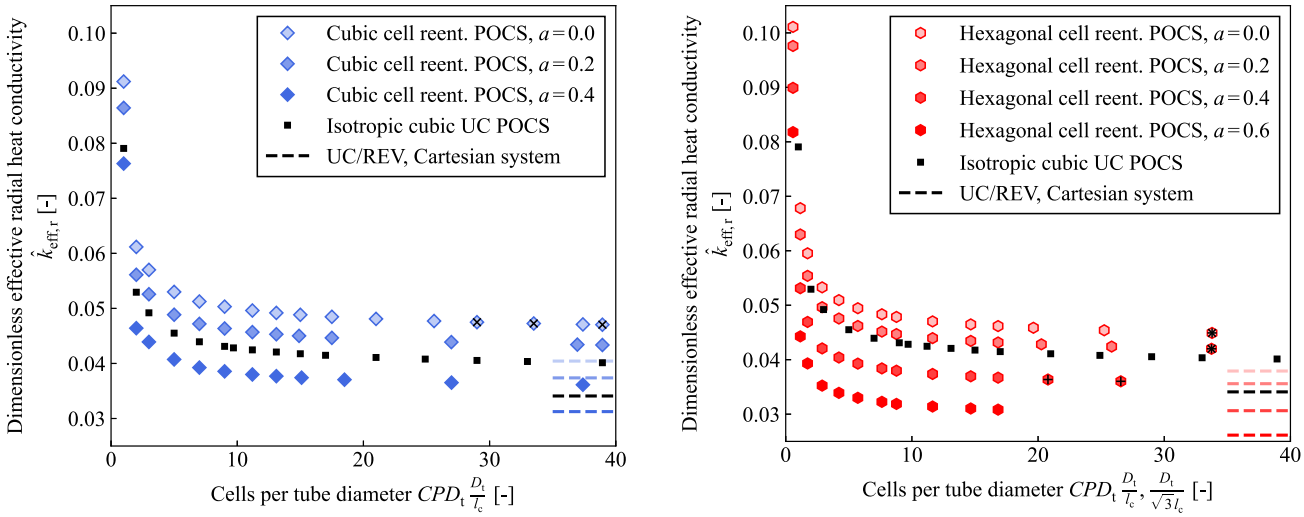

Figure 14. Effective radial heat conductivity in dimensionless form over CPD_t. $\hat{k}_{\mathrm{eff,r}}$ for cubic cell reentrant POCS (left) and for hexagonal cell reentrant POCS (right) are compared at the same solid fraction with $a = 0.0$. Isotropic cubic unit cell POCS serves as reference (black curve). Markers with × represent simulations with minor defects in meshing, using the element size category 3; markers with + represent simulations with the element size category 4 (see Table A2, Appendix A4). Combinations indicate data points, where simulations were performed with both element size categories. Effective heat conductivity related to the Cartesian system is indicated as horizontal dashed lines and is derived from simulations on the isotropic cubic unit cell (UC) and the reentrant structures' REVs, respectively.

are identical for all structures (negligible relative deviations of maximum 10^{-3}). All $\hat{k}_{\mathrm{eff,r}}$ reveal a hyperbolic trend and above ≈15 CPD_t the effective heat conductivity is approximately constant, only slightly decreasing. Especially at high CPD_t, the meshing process is challenging considering the small areas and volumetric bodies that result from the curved cut surface for the tube fitting. High amplitude factors impede the meshing further. Therefore, individual simulations were performed accepting minor defects in the mesh (e.g., where "edges are much shorter than the specified minimum element size"[43]), or with the element size category 4 for a higher resolution. In order to ensure reliable results, some simulations were performed twice using both mesh settings.

Further, we recognize two general influences: At first, as expected, a higher amplitude of the reentrant structures generally diminishes the effective radial heat conductivity. Second, not only for $a = 0.0$, but also for $a = 0.2$ the effective radial heat conductivity of both reentrant structures is higher than the isotropic cubic one. For $a = 0.0$, all considered structures reveal the same solid fraction, see Figure A12 in Appendix A4.2. However, in the case of the reentrant structures one half of the vertical strut is missing compared to the isotropic cubic unit cell POCS. Therefore, a higher portion of solid material contributes to the effective heat conduction in radial direction since struts are equally enlarged in diameter to meet the condition of an equal solid fraction. For the same reason, the cubic cell reentrant structure reveals a higher effective radial heat conductivity than the hexagonal one. In the case of the cubic cell reentrant structure, the vertical strut that is not contributing to radial heat conduction is thinner than the one within a hexagonal cell reentrant structure, cf., Table 3. Therefore, with the same solid fraction, the cubic cell reentrant structure reveals more solid material available for radial heat conduction.

Additionally, at $35 < CPD_t < 40$ the effective heat conductivity $\hat{k}_{\mathrm{eff,m}}$ of the isotropic unit cell and REVs of reentrant POCS, cf., Figure 6, are indicated as horizontal lines. For this, dedicated simulations were performed on the REVs with the same geometric parameters l_c, d_s, and a (Table 3). These values represent the effective heat conductivity of POCS in the radial plane, but based on the Cartesian system. Interestingly, even the threshold values in Figure 14 are well above the ones assigned to the Cartesian system—here, a factor between 1.15 and 1.18 applies.

For the effective radial heat conductivity $\hat{k}_{\mathrm{eff,r}}$, we postulate a hyperbolic correlation with CPD_t, including a dependency on the Cartesian values $\hat{k}_{\mathrm{eff,m}}$ in Equation (21):

$$\hat{k}_{\mathrm{eff,r}} = 0.033 \cdot (CPD_t)^{-1.08} + 1.2 \cdot \hat{k}_{\mathrm{eff,m,model}} \tag{21}$$

In case of the Cartesian effective heat conductivity, we apply the derived models $C_{x|y,m}$* for the cubic cell reentrant POCS and $H_{x|y,m}$* for the hexagonal cell reentrant POCS (see Table A3), as well as the empirical model by Bracconi et al. for the isotropic cubic unit cell POCS.[13] For the sake of a complete model, we further use the respective design equation of porosity, see Equation (4) and (6). For the isotropic cubic unit cell POCS, the design equation for porosity derived by Klumpp et al. is used.[48] The parameter estimation is based on the data for isotropic cubic unit cell and both reentrant POCS with $a = 0.0$. The resulting MAPE for the overall data is 4.72% and the parity plot is shown in **Figure 15**, including an error band of ±10%. The higher the CPD_t, the lower is $\hat{k}_{\mathrm{eff,r}}$, as well as the deviation from the simulation results and the deviation from $\hat{k}_{\mathrm{eff,m}}$. At last, the latter dependency holds for all structures investigated. This further affirms a general dependency of the effective heat conductivity on the solid fraction (while considering additional

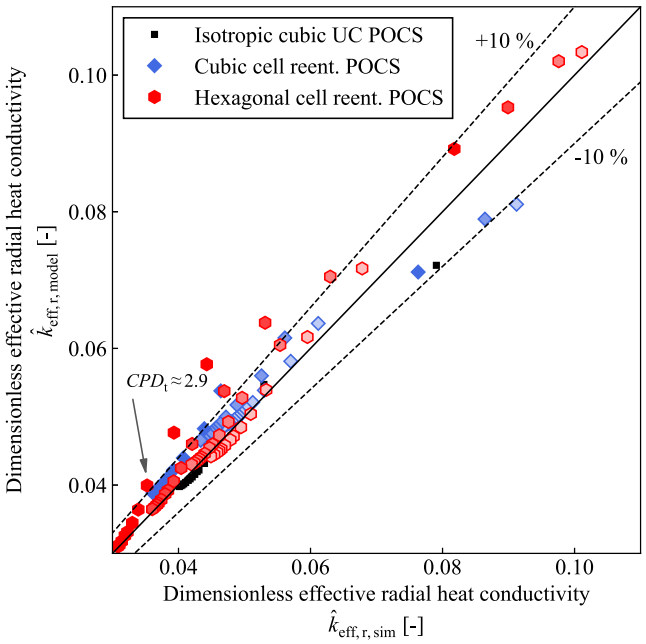

Figure 15. Parity plot for the effective radial heat conductivity of POCS, depending on the number of cell per tube diameter CPD_t, obtained from simulations and the model in Equation (21). The color intensity of the markers refers to the amplitude factor: light for $a = 0.0$ and strong for up to $a = 0.6$.

tortuosity in case of the reentrant POCS). High deviations of the model in Equation (21) are especially dominant for higher amplitude factors, but for $CPD_t > 3$ these are in the range of ±10%. For higher values of CPD_t, the solid fraction is approximately constant, whereas for low CPD_t fluctuations in the solid fraction occur (see Appendix A4.2). However, these fluctuations—most similar for all structures—have no direct influence on the curves depicted in Figure 14; neither do fluctuations in the proportion of the outer cut surface area S relative to the total outer surface area have an influence. The exemplary representation of the proposed model can be found in Appendix A4.2.

The most reasonable explanation for the decreasing trend of $\hat{k}_{\mathrm{eff,r}}$ with CPD_t is based on the transformation from Cartesian to polar coordinates. **Figure 16** shows the plot of the solid phase distribution of an arbitrary isotropic cubic cell structure with quadratic strut cross section in dimensionless Cartesian coordinates in comparison with polar coordinates. Here, up to $r/l_c = 1$ (i.e., $CPD_t = 2$) we can assume a combination of thermal resistances in parallel (if we neglect the centered vertical strut), while the struts virtually shrink in diameter. As described above, resistances in parallel reflect the upper bound, i.e., the lowest resistance in total, and a decreasing strut diameter hinders heat conduction. Moreover, assuming parallel heat flux lines, for $r/l_c > 1$ the increasing number of cells can be considered to additionally cause a network of serial connections that becomes more uniform with higher r/l_c, thus resulting in a decreased, but almost constant effective heat conductivity, cf., Figure 14. This asymptotic value of the effective radial heat conductivity is by a factor of ≈1.2 higher than the value obtained for a unit cell in one Cartesian direction. More data are required for $CPD_t \to \infty$, as the effective radial heat conductivity might approach the Cartesian value, representing the "original idea" of the representative unit cell. However, due to limitations in the meshing process and in numerics, more advanced investigations are required to validate this. Nevertheless, experimental investigations on POCS with $CPD_t > 40$ in chemical reactors are not known of so far. Moreover, a broad database regarding the effective radial heat conductivity of POCS built up from diverse unit cells is required to confirm the herewith presented behavior and the correlation proposed in Equation (21). Further note that this correlation holds for a constant effective radial heat conductivity over the tube radius, i.e., for a specified number of CPD_t. The herein presented relation must not be confused with a change of the effective radial heat conductivity of POCS over the normalized tube radius. However, the latter specification may be interesting for future investigations, in order to serve for a rigorous 2D modeling of tubular catalytic reactors.[51]

Serving as catalyst support structures, a high volume-specific surface area of POCS is usually beneficial for the catalytic performance. With the above finding, we can conclude that with increasing volume-specific surface area the effective radial heat conductivity decreases. For a fair comparison of the effective radial heat conductivity, we have to keep the solid fraction, and accordingly the characteristic ratio ϕ, constant. In order to increase the volume-specific surface area we choose a low strut diameter d_s and cell size l_c, cf., Equation (5) and (7). Consequently, for a fixed tube diameter the CPD_t is increasing and thus the effective radial heat conductivity is decreasing, see Figure 14.

In the preceding investigation, the characteristic ratio ϕ of the hexagonal cell reentrant POCS is ≈3.6, cf., Table 3. Using this design, **Figure 17** represents the decreasing effective radial heat conductivity with a decreasing cell size l_c from 15 to 3 mm in a tube with diameter $D_t = 50$ mm. This corresponds to ≈2–10 CPD_t. Ultimately, the decreasing cell size results in an increasing volume-specific surface area a_V, calculated by Equation (7), revealing a biobjective optimization problem. As we vary the amplitude factor a, we encounter a multiobjective optimization problem since the auxetic effect is more pronounced at higher amplitude factors, see part II.[41] With a large amplitude, the POCS itself would be more likely to establish a better interference fit in the tube and reveal a higher specific surface area, but a reduced effective radial heat conductivity. While it is possible to make general statements about the highest achievable effective heat conductivity, the optimal POCS design still depends on the particular application. Other important influencing factors include the chemical reaction system, flow conditions, and material properties.[3]

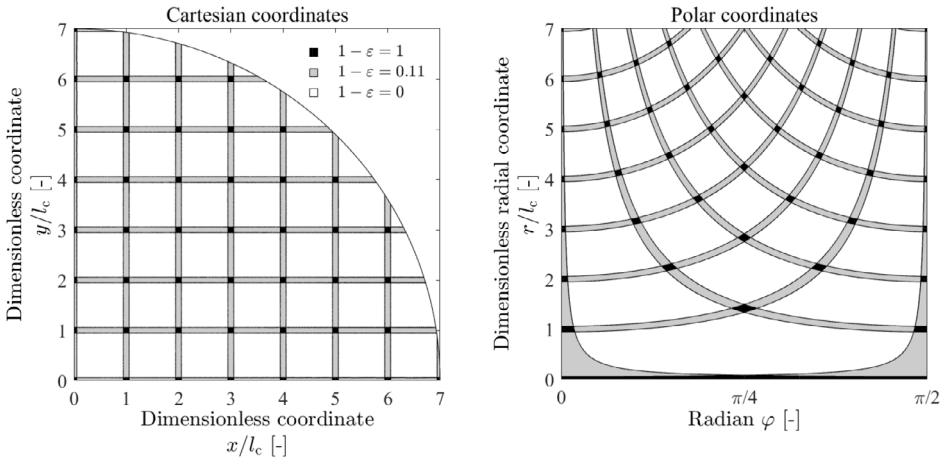

Figure 16. Local distribution of the solid fraction of an arbitrary, isotropic POCS with cubic unit cell, quadratic strut cross section, and $\phi = 8$. Presentation of the POCS in a quarter section of a tube with $CPD_t = 14$ in Cartesian coordinates (left) and in polar coordinates (right).

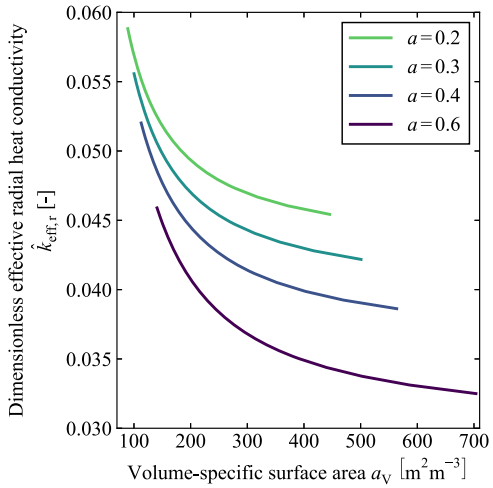

Figure 17. Dimensionless effective radial heat conductivity $\hat{k}_{\mathrm{eff,r}}$ of hexagonal cell reentrant POCS with $\phi = 3.6$ versus the volume-specific surface area a_V, corresponding to a varying number of cells per tube diameter CPD_t of ≈2–10 in a tube with diameter $D_t = 50$ mm. The amplitude factor a varies between 0.2 and 0.6.

In a final analysis, we assess the influence of CPD_t compared to that of the solid fraction on the effective radial heat conductivity of hexagonal cell reentrant POCS with $a = 0.2$. In **Figure 18**, the dimensionless effective radial heat conductivity $\hat{k}_{\mathrm{eff,r}}$ is plotted versus the volume-specific surface area a_V for a varied characteristic ratio ϕ in the range of 3–7. Note that this is an extrapolation of the above correlation in Equation (21), for which the underlying data refer to $3.6 \leq \phi \leq 5$ for a comparison of different POCS types at equal solid fraction. In the range of $5 < \phi \leq 7$, where the solid fraction changes only slightly (cf., Figure 5), the influence of CPD_t on $\hat{k}_{\mathrm{eff,r}}$ is of comparable extent as the influence of the change in solid fraction (≈35% change in $\hat{k}_{\mathrm{eff,r}}$). With lower ϕ, both the solid fraction and $\hat{k}_{\mathrm{eff,r}}$ rise drastically, and the influence of CPD_t is diminished (10% change in $\hat{k}_{\mathrm{eff,r}}$). Besides, with a higher solid fraction we obtain a broader range of a_V.

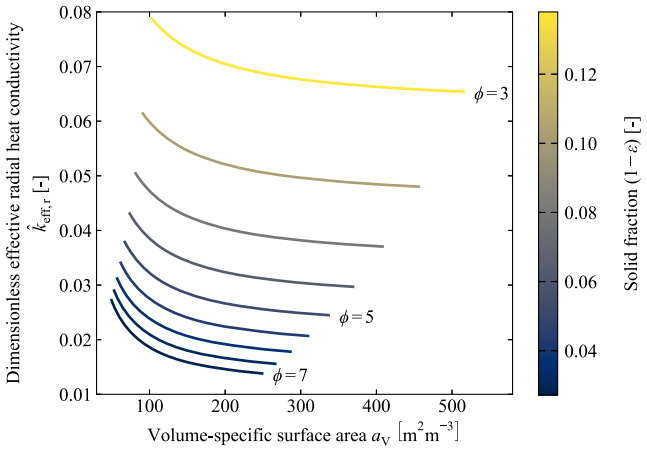

Figure 18. Dimensionless effective radial heat conductivity $\hat{k}_{\mathrm{eff,r}}$ of hexagonal cell reentrant POCS with $a = 0.2$ versus the volume-specific surface area a_V, corresponding to a varying number of cells per tube diameter CPD_t of ≈2–10 in a tube with diameter $D_t = 50$ mm. The characteristic ratio ϕ varies between 3 and 7; the resulting solid fraction is indicated via the color bar between 2.7 and 13.8%.

5. Summary and Conclusions

In this contribution, we present a thorough description and characterization of auxetic POCS regarding their design, geometrical description, and effective heat conductivity. Based on the auxetic reentrant mechanism using inverse hexagons, the cubic and the hexagonal cell types are investigated. Design equations regarding the morphological parameters porosity and volume-specific surface area are derived from the smallest repeatable units. The perspective application of such auxetic POCS in combination with a shape memory effect is for process intensification of chemical tubular reactors via an enhanced heat transfer across the tube wall. Hence, the application as well as the given anisotropy of reentrant structures predetermines the focus on the effective heat conductivity in the $x-y$-plane (radial plane) and the axial z-direction.

In order to assess the effective heat conductivity of these structures, numerical simulations were conducted using the software COMSOL Multiphysics. A rigorous mesh and discretization analysis resulted in a profound numerical approach that was validated with the literature data on isotropic POCS. Based on simulations using the REVs of reentrant POCS for heat conduction in one direction, a strong dependence of the effective heat conductivity on the solid fraction is confirmed. However, a geometry with pronounced auxetic behavior considerably diminishes the effective heat conductivity. The reason for this was found in the design of the auxetic curved struts. Although increasing the amplitude of the curved struts results in a higher solid fraction, the path of heat conduction is considerably lengthened. Furthermore, the anisotropic character of reentrant structures is reflected in a severely reduced effective heat conductivity in axial direction. A new correlation for the effective heat conductivity is proposed, considering the structures' solid volume fraction and the lengthened tortuous path of heat conduction in auxetic POCS. To come up with empirical models, we further drew distinctions between the cell type as well as the direction of heat conduction, i.e., the heat conduction in the radial plane and in axial direction.

Reentrant POCS with a cubic cell design exhibit a slightly higher effective radial heat conductivity than the ones with hexagonal cells. However, we assess the hexagonal cell design as favorable for a potential application in catalytic tubular reactors, justified by combining a better tubular fit with further advantages in design freedom, e.g., regarding the amplitude height, solid fraction, and stacking. Especially the stacking is expected to have a considerable effect on flow conditions, leading to a tuneable convective heat transfer. Part II of this study is dealing with the mechanical characterization of reentrant POCS and underlines this proposition.[41]

Moreover, spatially resolved investigations on the effective radial heat conductivity were performed by simulating heat conduction in cylindrical layers of conventional and auxetic POCS while changing the outer diameter. Thereby, a hyperbolic

dependency of the effective radial heat conductivity on the number of cells per tube diameter was determined. We expect this finding to be valid for structured, cellular materials in general (POCS, foams, monolithic honeycombs, and so on) and to our knowledge, it has not been reported before. A first correlation for the description of this behavior was set up, but has to be refined on a much broader database in a future study. Based on the available data, the hyperbolic threshold value is ≈20% higher than values obtained for effective heat conductivity in the Cartesian coordinate system. Concerning heat management, these findings can be fundamental in general for the application of open cellular structures in tubular reactors.

Appendix A

A1. Unit Cells of Cubic and Hexagonal Cell Reentrant POCS

In Figure A1, the representative unit cell of cubic cell reentrant POCS and in Figure A2 the representative unit cells of hexagonal cell reentrant POCS for the three different stackings are shown.

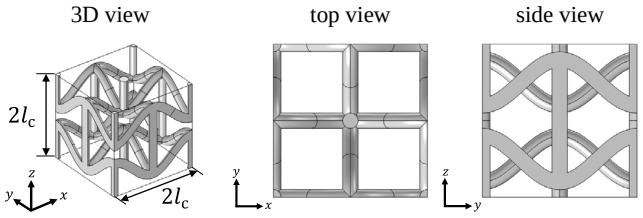

Figure A1. Representative unit cell of cubic cell reentrant POCS with $a = 0.3$.

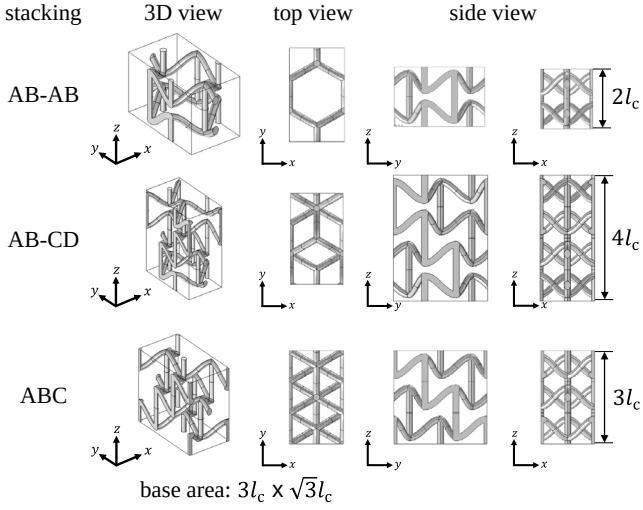

Figure A2. Representative unit cells of hexagonal cell reentrant POCS for the three different stackings with $a = 0.3$.

A2. Derivation of Theoretical Morphological Design Equations

In the following, we provide the detailed derivation of the design equations for porosity and volume-specific surface area of cubic and hexagonal cell reentrant POCS with curved struts. In general, we distinguish between struts and nodes, where the node consists of the overlapping solid volumes of the struts inside a corresponding cube (or prism in case of hexagonal cell type POCS) with the edge length of d_s. Moreover, inside the node space it is assumed that struts are not curved, but straight. Due to the reentrant characteristic, we have to consider two halves of the node: one with an overlapping vertical strut and one without.

The length of a vertical strut comprises half of the cell size l_c and the amplitude of the curved struts. However, we have to subtract $0.5 \cdot d_s$ since this length is already considered by the respective node volume. Finally, we set up the volume of a vertical strut as:

$$V_{s,vert} = \frac{\pi}{4} d_s^2 \left(\frac{l_c}{2} + a \cdot l_c - \frac{d_s}{2} \right) = \frac{\pi}{4} d_s^3 \left(\frac{\phi}{2} + \frac{\tilde{A}}{d_s} - \frac{1}{2} \right) \tag{A1}$$

The length of a curved strut $\mathcal{L}$ between the nodes is given by Equation (3), and the corresponding volume is:

$$V_{s,curved} = \frac{\pi}{4} d_s^2 \mathcal{L} \tag{A2}$$

A2.1 Cubic Cell Reentrant POCS

The node volume of cubic cell reentrant POCS comprises one half of the node of three overlapping cylinders $V_{node,3}$ and one half of the node of two overlapping cylinders $V_{node,2}$. Klumpp et al. derived the node volume of the first, which is the node volume of the isotropic cubic cell POCS:[48]

$$V_{node,3} = \left(\frac{3}{4}\pi - \sqrt{2} \right) d_s^3 \tag{A3}$$

The node volume of two overlapping struts can be expressed by the volume of two cylinders with the length d_s and diameter d_s minus the intersection volume of two orthogonal cylinders $V_{inter,\perp}$, i.e., a "Steinmetz" solid:

$$V_{node,2} = 2 \cdot V_{cyl} - V_{inter,\perp} = 2 \cdot \frac{\pi}{4} d_s^3 - \frac{2}{3} d_s^3 \tag{A4}$$

The complete node volume is:

$$V_{node,cub} = \frac{1}{2} \left(V_{node,3} + V_{node,2} \right) = \frac{d_s^3}{2} \left(\frac{5}{4}\pi - \left(\sqrt{2} + \frac{2}{3} \right) \right) \tag{A5}$$

The overall solid volume $V_{S,cub}$ defined by the smallest repeatable unit of the cubic cell reentrant POCS (cf., Figure 4) is:

$$V_{\mathrm{S,cub}} = 1 \cdot V_{\mathrm{s,vert}} + 2 \cdot V_{\mathrm{s,curved}} + 1 \cdot V_{\mathrm{node,cub}} = \frac{d_\mathrm{s}^3}{8}\left[\pi\phi + \frac{\pi}{d_\mathrm{s}}\left(2\tilde{A} + 4\mathcal{L}\right) + 4\pi - \left(4\sqrt{2} + \frac{8}{3}\right)\right] \tag{A6}$$

The volume of the smallest repeatable unit of the cubic cell reentrant POCS is $V_{\mathrm{SRU,cub}} = l_\mathrm{c}^3$ and further the porosity is defined as follows:

$$\begin{aligned}\varepsilon_{\mathrm{cub}} &= 1 - \frac{V_{\mathrm{S,cub}}}{V_{\mathrm{SRU,cub}}} \\ &= 1 - \frac{d_\mathrm{s}^3}{8 l_\mathrm{c}^3}\left[\pi\left(\phi + \underbrace{\frac{2}{d_\mathrm{s}}\left(\tilde{A} + 2\mathcal{L}\right)}_{B_{\mathrm{cub}}}\right) + 4\left(\pi - \left(\sqrt{2} + \frac{2}{3}\right)\right)\right] \\ &= 1 - \frac{\pi(\phi + B_{\mathrm{cub}}) + 4 \cdot \left(\pi - \left(\sqrt{2} + \frac{2}{3}\right)\right)}{8\phi^3}.\end{aligned} \tag{A7}$$

Furthermore, Klumpp et al. derived a formula for the surface area of the isotropic cubic cell node:[48]

$$A_{\mathrm{node},3} = 12 \cdot \left(\frac{\pi}{4} - \frac{1}{\sqrt{2}}\right) d_\mathrm{s}^2 \tag{A8}$$

In their contribution, they present a methodology to accurately determine the surface area of cut cylinders by integral calculus.[48] In the following, we adapted this for the surface area of two crossing cylinders, i.e., the surface area of the node's second half of cubic cell reentrant structures. For the triangular lateral surface of a cut strut, the following applies:

$$A_{\mathrm{tri,cross}} = \frac{\pi}{2} r_\mathrm{s}^2 - \int_0^{\frac{\pi}{2} r_\mathrm{s}} r_\mathrm{s} \cos\left(\frac{u}{r_\mathrm{s}}\right) \mathrm{d}u \tag{A9}$$

with u as the perimeter of a cylinder. We solve the integral to receive the final equation:

$$\begin{aligned}A_{\mathrm{tri,cross}} &= \frac{\pi}{2} r_\mathrm{s}^2 - r_\mathrm{s}\left[\sin\left(\frac{u}{r_\mathrm{s}}\right) r_\mathrm{s}\right]_0^{\frac{\pi}{2} r_\mathrm{s}} \\ &= r_\mathrm{s}^2\left(\frac{\pi}{2} - 1\right)\end{aligned} \tag{A10}$$

The node surface consists of 16 of such identical areas. Hence, it sums up to:

$$\begin{aligned}A_{\mathrm{node},2} &= 16 A_{\mathrm{tri,cross}} \\ &= 4 \cdot \left(\frac{\pi}{2} - 1\right) d_\mathrm{s}^2\end{aligned} \tag{A11}$$

For the node's total surface of a cubic cell reentrant structure, we receive:

$$\begin{aligned}A_{\mathrm{node,cub}} &= \frac{1}{2}\left(A_{\mathrm{node},2} + A_{\mathrm{node},3}\right) \\ &= \left(\frac{5}{2}\pi - \left(2 + 3\sqrt{2}\right)\right) d_\mathrm{s}^2\end{aligned} \tag{A12}$$

The overall surface area defined by the cubic cell reentrant structure's smallest repeatable unit is:

$$A_{\mathrm{cub}} = 1 \cdot A_{\mathrm{s,vert}} + 2 \cdot A_{\mathrm{s,curved}} + 1 \cdot A_{\mathrm{node,cub}} = \frac{d_\mathrm{s}^2}{2}\left[\pi\phi + \pi\underbrace{\frac{2}{d_\mathrm{s}}\left(\tilde{A} + 2\mathcal{L}\right)}_{B_{\mathrm{cub}}} + 4\pi - \left(4 + 6\sqrt{2}\right)\right] \tag{A13}$$

The overall volume-specific surface area with regard to the volume of the smallest repeatable unit of the cubic cell reentrant structure $V_{\mathrm{SRU,cub}} = l_\mathrm{c}^3$ calculates as:

$$\begin{aligned}a_{\mathrm{V,cub}} &= \frac{A_{\mathrm{cub}}}{V_{\mathrm{SRU,cub}}} \\ &= \frac{\pi(\phi + B_{\mathrm{cub}}) + 4 \cdot \left(\pi - \left(\frac{3}{2}\sqrt{2} + 1\right)\right)}{2\phi^2 l_\mathrm{c}}\end{aligned} \tag{A14}$$

A2.2 Hexagonal Cell Reentrant POCS

As for the cubic cell reentrant POCS, it makes sense to start with the node. Again, the node volume consists of half of the node of a conventional, hexagonal cell non-reentrant structure $V_{\mathrm{node,hex*}}$, cf., Figure A3, left, and half of the node of a planar triplet of cylinders, with an angle of 120° in between, $V_{\mathrm{node,triple}}$. To derive the design equation of the volume (and hence, porosity) of the structures, it is crucial to consider the cylinder volumes and the overlapping spaces.

For both nodes, the triplet cylinders each have a length of $0.5 \cdot d_\mathrm{s}$ and meet in the center, which the three respective axes build. The total volume of the hexagonal cell non-reentrant node is the volume of the vertical cylinder plus the volume of the planar cylinder triplet minus the threefold of half the intersection volume $V_{\mathrm{inter},\perp}$. This considers the intersection volume of the vertical cylinder with each of the planar cylinders, see Figure A3, right. Moreover, the remaining intersection volumes of the triplet cylinders have to be considered, which is depicted edged red in Figure A4. In the following, this intersection is denoted as "cap":

$$V_{\mathrm{node,hex*}} = V_{\mathrm{cyl,vert}} + 3 \cdot V_{\mathrm{cyl,planar}} - 3 \cdot \frac{1}{2} V_{\mathrm{inter},\perp} - 3 \cdot V_{\mathrm{cap}} \tag{A15}$$

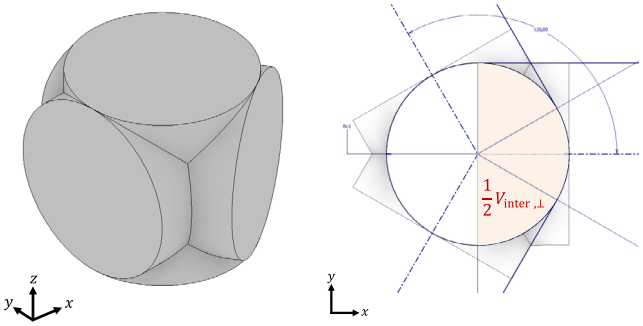

Figure A3. Node of the conventional, hexagonal cell non-reentrant structure. Left: 3D view, right: top view, including the depiction of half of the intersection of two orthogonal struts $V_{\mathrm{inter},\perp}$, i.e., the vertical strut in z-direction and the strut in x-direction.

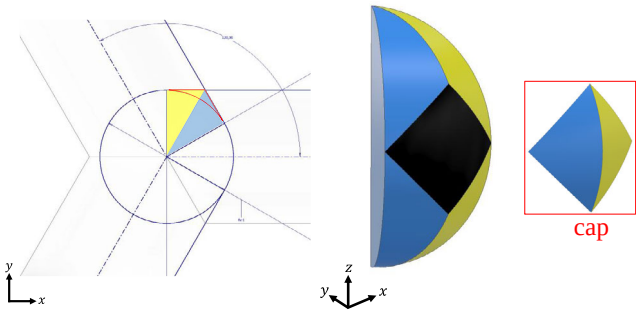

Figure A4. Detailed representation of one of the three identical intersections in a hexagonal cell structure's node, formed by a planar cylinder triplet.

Geometrically, the cap can be described as follows: Initially, we neglect the vertical cylinder. Then, we receive three of the identical blue–yellow intersections in Figure A4. Each single, yellow or blue intersection with $V_{\text{half}-\text{cyl},30°}$, is a simple cutout piece of a half cylinder in a 30° angle:

$$\begin{aligned}\frac{V_{\text{half}-\text{cyl},30°}}{2} &= \int_{x_1=0}^{r_s}\int_{x_2=0}^{\sqrt{r_s^2-x_1^2}}\int_{x_3=0}^{\frac{\sqrt{3}}{3}x_2} 1\,\mathrm{d}x_3\,\mathrm{d}x_2\,\mathrm{d}x_1 \\ &= \frac{\sqrt{3}}{9}r_s^3 \\ &= \frac{\sqrt{3}}{72}d_s^3\end{aligned} \tag{A16}$$

Hence, the total, blue–yellow intersection in Figure A4, right, including the cap, is:

$$\begin{aligned}V_{\text{inter,b}-\text{y}} &= 2\cdot V_{\text{half}-\text{cyl},30°} \\ &= \frac{\sqrt{3}}{18}d_s^3\end{aligned} \tag{A17}$$

Later, we will compute the cap's volume as the remainder of a subtraction. Therefore, we consider now the vertical cylinder, and similar to the previous step, we calculate the 30° cutout of the intersection volume of two orthogonal cylinders $V_{\text{inter},\perp}$. Graphically, this is the intersection of the red-shaded space in Figure A3 and the yellow (or blue) space in Figure A4, left. For calculation, we consider only one octant in the reference coordinate system. Thus, we receive the volume of one quarter of the intersection, without the cap (Figure A4, middle):

$$\begin{aligned}\frac{V_{\text{inter,hex}}}{4} &= \int_{x_1=0}^{r_s}\int_{x_2=0}^{\sqrt{r_s^2-x_1^2}}\int_{x_3=0}^{\sqrt{r_s^2-x_1^2}} 1\,\mathrm{d}x_3\,\mathrm{d}x_2\,\mathrm{d}x_1 \\ &\quad - \int_{x_1=0}^{\frac{\sqrt{3}}{2}r_s}\int_{x_2=0}^{\sqrt{r_s^2-x_1^2}}\int_{x_3=\frac{\sqrt{3}}{3}x_1}^{\sqrt{r_s^2-x_1^2}} 1\,\mathrm{d}x_3\,\mathrm{d}x_2\,\mathrm{d}x_1 \\ &= \frac{2}{3}r_s^3 - \left(3-\frac{7}{9}\right)\frac{\sqrt{3}}{8}r_s^3 \;= \frac{2}{3}\left(1-\frac{5}{12}\sqrt{3}\right)r_s^3 \\ &= \frac{1}{12}\left(1-\frac{5}{12}\sqrt{3}\right)d_s^3\end{aligned} \tag{A18}$$

For the volume of the cap, we receive:

$$\begin{aligned}V_{\text{cap}} &= V_{\text{inter,b}-\text{y}} - V_{\text{inter,hex}} \\ &= \left[\frac{\sqrt{3}}{18} - \frac{1}{3}\left(1-\frac{5}{12}\sqrt{3}\right)\right]d_s^3 \\ &= \left(\frac{7}{36}\sqrt{3}-\frac{1}{3}\right)d_s^3\end{aligned} \tag{A19}$$

With Equation (A15), the volume of the node results in:

$$V_{\text{node,hex}*} = \left(\frac{5}{8}\pi - \frac{7}{12}\sqrt{3}\right)d_s^3 \tag{A20}$$

The node volume of the cylinder triplet $V_{\text{node,triple}}$ is much easier to derive now. Three times the cylinder volume with $l_c = 0.5\cdot d_s$ minus three times the blue–yellow intersection $V_{\text{inter,b}-\text{y}}$:

$$V_{\text{node,triple}} = 3\cdot\left(\frac{\pi}{8} - \frac{\sqrt{3}}{18}\right)d_s^3 \tag{A21}$$

Eventually, the node volume of the hexagonal cell reentrant structure results in

$$\begin{aligned}V_{\text{node,hex}} &= \frac{1}{2}\left(V_{\text{node,hex}*} + V_{\text{node,triple}}\right) \\ &= \frac{1}{2}\left(\pi - \frac{3}{4}\sqrt{3}\right)d_s^3\end{aligned} \tag{A22}$$

The overall solid volume $V_{\text{S,hex}}$ defined by the smallest repeatable unit of the hexagonal cell reentrant POCS (cf., Figure 4) is:

$$\begin{aligned}V_{\text{S,hex}} &= 2\cdot\frac{1}{6}\cdot V_{\text{s,vert}} + \frac{1}{2}\cdot V_{\text{s,curved}} + 2\cdot\frac{1}{6}\cdot V_{\text{node,hex}} \\ &= \frac{d_s^3}{6}\left[\frac{\pi}{4}\phi + \underbrace{\frac{\pi}{4}\frac{1}{d_s}\left(2\tilde{A}+3\mathcal{L}\right)}_{B_{\text{hex}}} + \frac{3}{4}\left(\pi-\sqrt{3}\right)\right]\end{aligned} \tag{A23}$$

The volume of the smallest repeatable unit of the hexagonal cell reentrant POCS is $V_{\text{SRU,hex}} = \frac{\sqrt{3}}{4}l_c^3$ and further the porosity is defined as follows:

$$\begin{aligned}\varepsilon_{\text{hex}} &= 1 - \frac{V_{\text{S,hex}}}{V_{\text{SRU,hex}}} = 1 - \frac{2}{3}\frac{d_s^3}{\sqrt{3}l_c^3}\left[\frac{\pi}{4}\phi + \frac{\pi}{4}B_{\text{hex}} + \frac{3}{4}\left(\pi-\sqrt{3}\right)\right] \\ &= 1 - \frac{\sqrt{3}}{18\phi^3}\left[\pi(\phi+B_{\text{hex}}) + 3\left(\pi-\sqrt{3}\right)\right] \\ &= 1 - \frac{\sqrt{3}\pi(\phi+B_{\text{hex}}) + \sqrt{3}\cdot 3\pi - 9}{18\phi^3}\end{aligned} \tag{A24}$$

In order to determine the volume-specific surface area of hexagonal cell reentrant structures, we start again with the surface area of the node, and again, apply the method presented by Klumpp et al.[48] Here, we directly determined the surface area of the hexagonal cell node, which consists of four different areas:

$$A_{\text{node,hex}} = 3A_1 + 12A_2 + 6A_3 + 6A_4 \tag{A25}$$

Each of the areas represents triangular surfaces of a cut strut, similar to above. The exception is A_1 that is a stripe with a partial circumference, see Figure A5.

For the areas A_2–A_4, we receive:

$$\begin{aligned} A_2 &= \frac{\pi}{3}r_s^2 - \int_0^{\frac{\pi}{3}r_s} r_s \cos\left(\frac{u}{r_s}\right) \mathrm{d}u \;= r_s^2\left(\frac{\pi}{3} - \frac{\sqrt{3}}{2}\right) \\ A_3 &= \frac{\pi}{2}\frac{\sqrt{3}}{3}r_s^2 - \int_0^{\frac{\pi}{2}r_s} \frac{\sqrt{3}}{3} r_s \cos\left(\frac{u}{r_s}\right) \mathrm{d}u \;= \frac{\sqrt{3}}{3}r_s^2\left(\frac{\pi}{2} - 1\right) \\ A_4 &= \frac{\pi}{6}\frac{\sqrt{3}}{3}r_s^2 - \int_0^{\frac{\pi}{6}r_s} \frac{\sqrt{3}}{3} r_s \cos\left(\frac{u}{r_s}\right) \mathrm{d}u \;= \frac{\sqrt{3}}{3}r_s^2\left(\frac{\pi}{6} - \frac{1}{2}\right) \end{aligned} \tag{A26}$$

From the calculation of A_2, we receive the height h of the triangle, which is

$$h = r_s - \cos\left(\frac{\pi}{3}\right) r_s = \frac{r_s}{2} \tag{A27}$$

and further determines the partial circumference u_1 to calculate A_1:

$$\begin{aligned} u_1 &= 2\pi r_s\left(1 - \frac{\cos^{-1}\left(\frac{h}{r_s}\right)}{180°}\right) \;= \frac{4}{3}\pi r_s \\ A_1 &= \frac{4}{3}\pi r_s^2\left(1 - \frac{\sqrt{3}}{3}\right) \end{aligned} \tag{A28}$$

Finally, the surface area of the hexagonal cell reentrant structure's node is:

$$A_{\text{node,hex}} = \left(2\pi - \frac{9}{4}\sqrt{3}\right) d_s^2 \tag{A29}$$

The surface area A_{hex} of the solid inside the smallest repeatable unit (cf., Figure 4) is:

$$\begin{aligned} A_{\text{hex}} &= 2 \cdot \frac{1}{6} \cdot A_{\text{s,vert}} + \frac{1}{2} \cdot A_{\text{s,curved}} + 2 \cdot \frac{1}{6} \cdot A_{\text{node,hex}} \\ &= \frac{d_s^2}{6}\left[\pi\phi + \pi \underbrace{\frac{1}{d_s}\left(2\tilde{A} + 3\mathcal{L}\right)}_{B_{\text{hex}}} + 3\pi - \frac{9}{2}\sqrt{3}\right] \end{aligned} \tag{A30}$$

The volume of the smallest repeatable unit of the hexagonal cell reentrant POCS is $V_{\text{SRU,hex}} = \frac{\sqrt{3}}{4} l_c^3$ and further the volume-specific surface area is defined as follows:

$$\begin{aligned} a_{\text{V,hex}} &= \frac{A_{\text{hex}}}{V_{\text{SRU,hex}}} = \frac{4A_{\text{hex}}}{\sqrt{3}l_c^3} \\ &= \frac{2\sqrt{3}\pi(\phi + B_{\text{hex}}) + \sqrt{3} \cdot 6\pi - 27}{9\phi^2 \cdot l_c} \end{aligned} \tag{A31}$$

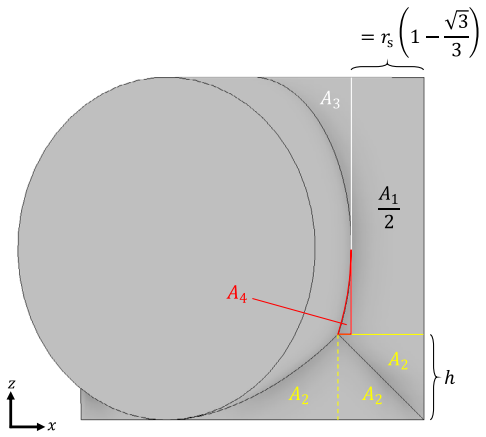

Figure A5. Depiction of the hexagonal cell reentrant structure's node as side view, including the division into the four areas A_1 to A_4.

A3. Mesh and Discretization Analysis

The isotropic cubic unit cell and the hexagonal cell reentrant POCS are used for the mesh and discretization analysis. Solely the x-direction was considered for the hexagonal cell reentrant structure for mesh and discretization analysis. Therefore, half of the REV in Figure 6 (right) was used, realized by a cut at 0.5 L_y along the x–z-plane. Hence, computational effort is decreased and no periodic condition is (mathematically) needed. We make the assumption that the following quality assessment holds for all structures comprised in this work, along with the REVs shown in Figure 6. The preliminary investigation covers the parameter variations given in Table A1.

For the mesh and discretization analysis, variations in element size and order of shape function are necessary. In this work, the predefined "physics-controlled mesh" element size categories were applied and numbers have been assigned accordingly, see Table A2. Element size category 1 is the "normal" one: for lower numbers the element sizes get bigger (and the mesh becomes coarser) and for higher numbers the mesh becomes finer. With "Advanced Physics Options," the order of discretization of the elements, i.e., the order of the base function, as well as the base function itself can be adjusted. In this work, only the nodal Lagrange base function ("shape function") is considered.[43]

The Lagrange shape functions of second, third, and fourth order, namely, "quadratic," "cubic," and "quartic" Lagrange were selected, resulting in 92 and 176 single simulations for the

Table A1. Variations in geometry parameters for mesh and discretization analysis.

Structure	Cell size l_c [mm]	Strut diameter d_s [mm]	Characteristic ratio ϕ [–]	Amplitude factor a [–]
Isotropic cubic	3	{0.2, 1.0}	{15, 3}	–
	5		{25, 5}	–
Reentrant hexagonal	3	{0.2, 1.5}	{15, 2}	{0.1, 0.8}
	5		{25, 3.$\bar{3}$}	

Table A2. Predefined "physics-controlled mesh" element size categories in COMSOL Multiphysics.[43]

Element size category	Minimum to maximum element size [mm]	Assigned number
Extra coarse	0.2700–1.5000	−2
Coarser	0.2000–0.9500	−1
Coarse	0.1400–0.7500	0
Normal	0.0900–0.5000	1
Fine	0.0500–0.4000	2
Finer	0.0200–0.2750	3
Extra fine	0.0075–0.1750	4
Extremely fine	0.0010–0.1000	5

isotropic cubic unit cell and hexagonal cell reentrant structure, respectively. Subsequently, $\hat{k}_{\text{eff}}$ values were determined and further processed in order to determine configurations leading to divergence due to a bad condition or round-off errors. For this, the squared deviations of $\hat{k}_{\text{eff}}$ from the one of the respective previous element size category were determined. In general, this deviation should constantly decrease with higher spatial resolution. Moreover, the squared deviations of $\hat{k}_{\text{eff}}$ from the one of the most coarse element size category were determined. For increased spatial resolution, these should increase and reach an asymptotic value. At last, $\hat{k}_{\text{eff}}$ values were normalized to the ones of a reference element size category, representing the one with highest precision, as identified by the preceding analysis.

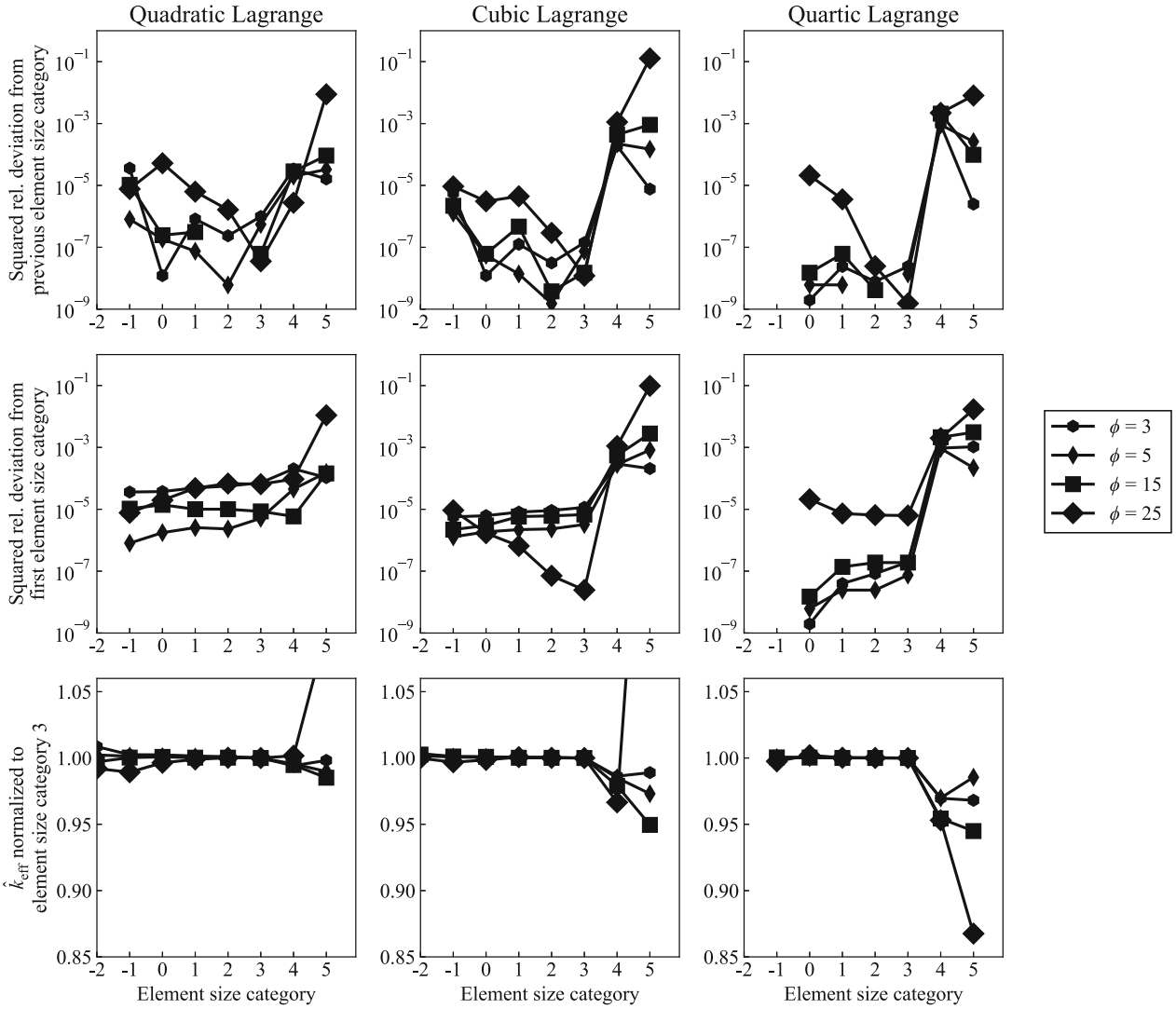

Figure A6. Analysis of the dimensionless effective heat conduction depending on element size category and discretization order for the isotropic cubic unit cell. Element size category: 1 is the "normal" element size category, for higher numbers the mesh becomes finer, i.e., elements become smaller. Data points are connected in order to indicate the trend.

The analysis results are shown in Figure A6 for the isotropic cubic unit cell and in Figure A7 for the hexagonal cell reentrant structure. In general, with a higher order in the Lagrange shape function, the deviations in $\hat{k}_{\text{eff}}$ get smaller, and for high ϕ a finer mesh resolution has a greater positive effect, which can be explained by the low d_s for high ϕ (here: 0.2 mm). However, for the investigated structures, divergence of simulation results can be clearly identified and seem to be independent of the order of the base functions, respectively. In case of the hexagonal cell reentrant structures divergence of the simulation results is dominant for the element size category 5, whereas for the isotropic cubic unit cell divergence occurs already for category 4.

Thus, for all simulations presented in this contribution the element size category 3 is chosen along with the shape function "quartic Lagrange." On the one hand, this is a compromise with regard to accuracy requirements and to guaranteeing a fair comparison between reentrant and isotropic structures, and thereby to the literature data, cf., Section 3.1. On the other hand, simulations of reentrant structures are expected to be robust since the simulations are performed distant from the practical limit given by the element size category, and to be sufficiently accurate, since a high order of the base function is applied.

In order to ensure the prediction of the POCS' specific properties by the REV, a fivefold of the calculation domains used for the mesh and discretization analysis, i.e., five units in series, was studied for an extended range in parameter combinations.[13] For the isotropic cubic unit cell, d_s was varied in 0.2 mm intervals between 0.2 and 1.4 mm for $l_c = \{3, 5\}$ mm. Relative deviations between one and five unit cells of $\hat{k}_{\text{eff}}$ are less than 0.022% (mean 0.009%). For the hexagonal cell reentrant unit, d_s was varied in 0.2 mm intervals between 0.2 and 1.4 mm, a was varied in 0.2 intervals between 0.0 and 0.8 for $l_c = 5$ mm. Relative deviations of $\hat{k}_{\text{eff}}$ are less than 1.150% (mean 0.402%).

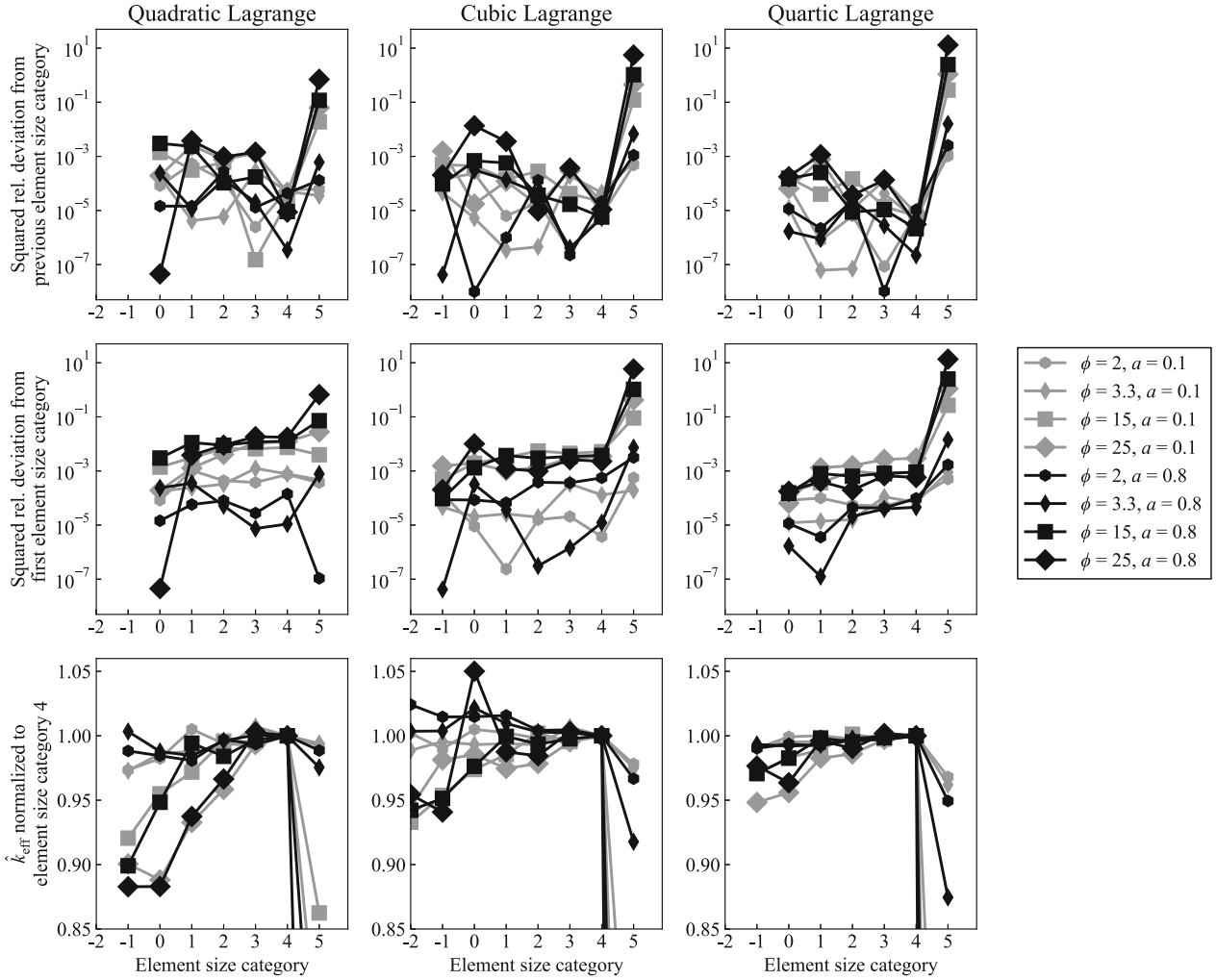

Figure A7. Analysis of the dimensionless effective heat conduction depending on element size category and discretization order for the REV of hexagonal cell reentrant structure. Element size category: 1 is the "normal" element size category, for higher numbers the mesh becomes finer, i.e., elements become smaller. Data points are connected in order to indicate the trend.

A4. Further Model Results

For model $H_{x|y,m}$ of hexagonal cell reentrant POCS, Figure A8 shows the parity plot for the dimensionless effective heat conductivity $\hat{k}_{\mathrm{eff},\mathrm{m,hex}}$ with an error band of ±15% for all geometry parameter combinations with $\phi \geq 3$. However, a slight systematic drift is recognizable.

Figure A9 shows the parity plot for model H_z of the effective heat conductivity in z-direction of hexagonal cell reentrant POCS with an error band of ±20% for all geometry parameter combinations with $\phi \geq 3$. The overestimation in the range of interest can be clearly seen in Figure A10.

A4.1 Reparameterized Correlations in Cartesian System

In order to account for the systematic deviation in the presented model above, a reparameterization is done for the narrowed range of interest of geometric parameters, cf., Table 5, but including amplitude factors $a = \{0.0, 0.1\}$. This range represents combinations of the geometry parameters that will be used in upcoming investigations on auxetic POCS applied as catalyst carriers. The corresponding results can be found in Table A3 and are depicted for the hexagonal design with $\hat{k}_{\mathrm{eff},\mathrm{m}}$ in the radial plane in Figure A11.

A4.2 Effective Radial Heat Conductivity

Figure A12 shows the solid fraction of all investigated POCS over the number of cells per tube diameter CPD_t. Above $CPD_t \approx 5$, the solid fraction is approximately constant and corresponds to the value derived from the smallest repeatable unit (cf., Appendix A2).

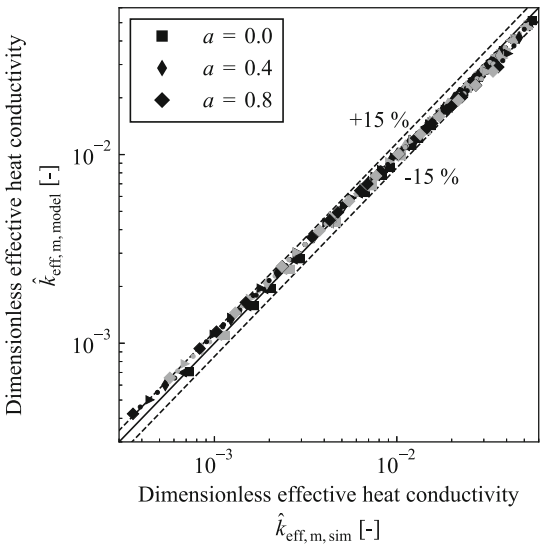

Figure A8. Parity plot for model $H_{x|y,m}$ (radial plane) of hexagonal cell reentrant POCS with an error band of ±15 % and the total dataset of $\hat{k}_{\mathrm{eff},\mathrm{m,hex}}$ with $\phi \geq 3$. The black markers refer to datasets with $l_c = \{3, 5\}$ mm; gray markers indicate the independent dataset with $l_c = 4$ mm. The circles • are displaying $\hat{k}_{\mathrm{eff}}$-values for intermediate amplitude factors a.

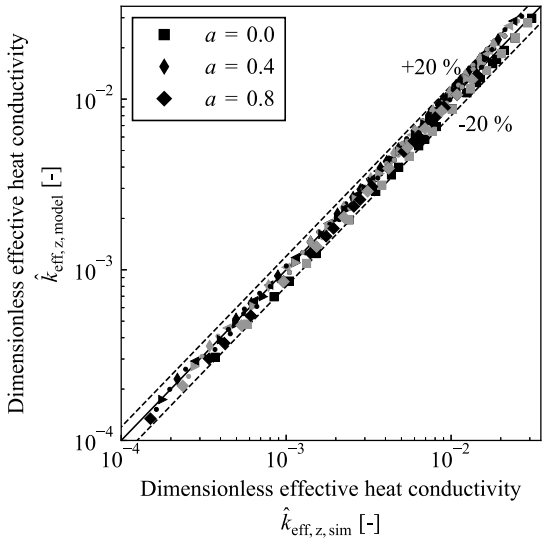

Figure A9. Parity plot for model H_z (axial direction) of hexagonal cell reentrant POCS with an error band of ±20 % and the total dataset of $\hat{k}_{\mathrm{eff},\mathrm{z,hex}}$ with $\phi \geq 3$. The black markers refer to datasets with $l_c = \{3, 5\}$ mm; gray markers indicate the independent dataset with $l_c = 4$ mm. The circles • are displaying $\hat{k}_{\mathrm{eff}}$-values for intermediate amplitude factors a.

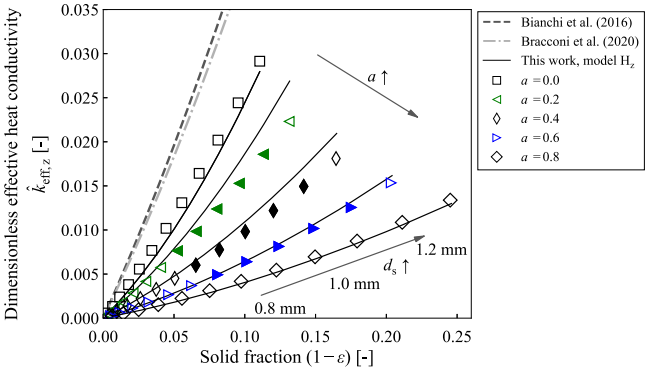

Figure A10. Effective heat conductivity in dimensionless form in the axial direction $\hat{k}_{\mathrm{eff,z}}$ for the hexagonal cell reentrant structure. Results obtained by simulations using $l_c = 4$ mm as independent data are indicated as markers. Filled markers represent data within the narrowed range of interest, cf., Table 5. Curves represent the model correlation H_z developed within this work and the literature correlations as reported.[12,13]

Figure A13 shows the representation of the proposed model of the effective radial heat conductivity in Equation (21). For the isotropic cubic unit cell POCS and the hexagonal cell reentrant POCS with $a = 0.0$, the effective radial heat conductivity is slightly underestimated; for cubic cell reentrant POCS with $a = 0.0$, the model reveals an appropriate fit. However, the parameter estimation is based on these simulation data. For independent data of the reentrant POCS with varying amplitude factor a, we refer to the parity plot in Figure 15.

Table A3. Results of the reparameterization of α and β corresponding to Equation (18) for the narrowed range of interest (including $a = \{0.0, 0.1\}$), MAPE with respect to the independent data, with $l_c = 4$ mm.

Reentrant structure	Domain	Empirical parameters		MAPE[a)] [%]	Model abbreviation
		α [–]	β [–]		
Cubic	Radial plane	0.43	1.91	1.64	$C_{x\|y,m}$*
	Axial direction z	0.11	4.03	9.65	C_z*
Hexagonal	Radial plane	0.38	1.81	2.79	$H_{x\|y,m}$*
	Axial direction z	0.15	2.45	6.39	H_z*

[a)]MAPE for the narrowed range of interest in geometry parameters, including $a = \{0.0, 0.1\}$.

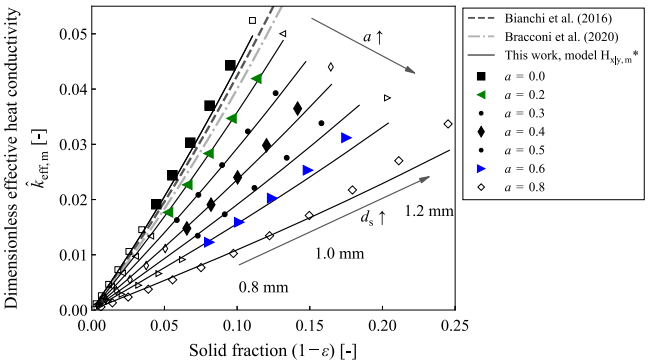

Figure A11. Averaged effective heat conductivity in dimensionless form in the radial plane $\hat{k}_{\mathrm{eff,m}}$ for the hexagonal cell reentrant POCS. Results obtained by simulations using $l_c = 4$ mm as independent data are indicated as markers. Filled markers represent data within the narrowed range of interest, including $a = \{0.0, 0.1\}$. Curves represent the model correlation $H_{x|y,m}$* developed within this work and literature correlations as reported.[12,13]

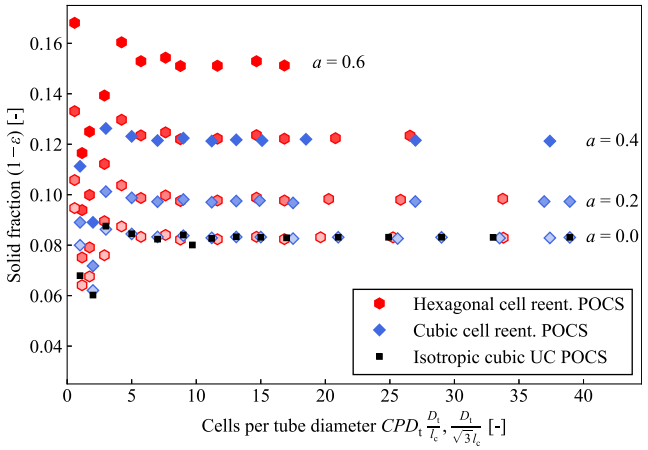

Figure A12. Solid fraction of all investigated POCS over CPD_t. The color intensity of the markers refers to the amplitude factor as indicated.

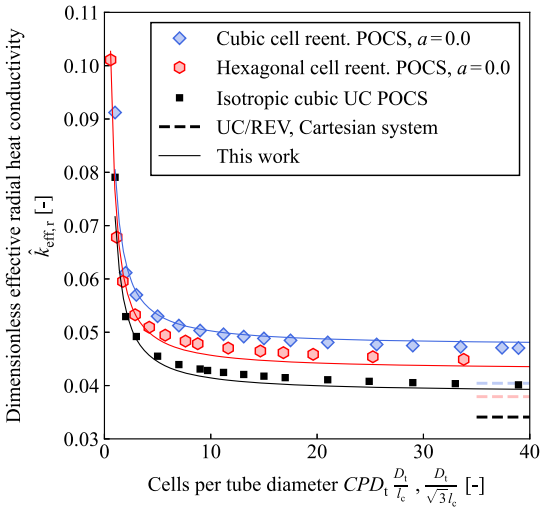

Figure A13. Effective radial heat conductivity in dimensionless form over CPD_t. $\hat{k}_{\mathrm{eff,r}}$ for cubic cell, hexagonal cell reentrant POCS with $a = 0.0$, and isotropic cubic unit cell POCS are compared at the same solid fraction. Effective heat conductivity related to the Cartesian system is indicated as horizontal dashed lines and is derived from simulations on the isotropic cubic UC and the REVs of the reentrant structures, respectively.

Nomenclature

Latin symbols		
a	–	Amplitude factor
a_V	m^2m^{-3}	Volume-specific surface area
$\tilde{A}$	m	Amplitude of curved struts
A	m^2	Area
B	–	Auxiliary parameter
d_s	m	Strut diameter
D	m	Diameter
f	–	Factor of cutout fraction
h	m	Height of a triangular lateral surface
H	m	Height of POCS
k	$Wm^{-1}K^{-1}$	Heat conductivity
$\hat{k}$	–	Dimensionless heat conductivity
l_c	m	Cell size
L	m	Distance between two isothermal faces
$\mathcal{L}$	m	Effective length of curved struts
r	m	Radius
S	m^2	Area of the cut surface, corresponding to the obtained heat flux
T	K	Temperature
u	m	circumference
V	m^3	Volume
q	Wm^{-2}	(Conductive) heat flux
Q	W	(Conductive) heat flow
Greek symbols		
α	–	Empirical parameter
β	–	Empirical parameter

ΔT	K	Temperature difference
ε	–	Porosity
τ	–	Tortuosity
ϕ	–	Characteristic ratio
φ	–	Radian
Abbreviations		
CAD		Computer-aided design
CPD_t		Cells per tube diameter
MAPE		Mean absolute percentage error
PBF-EB		Electron beam powder bed fusion
POCS		Periodic open cellular structures
REV		Representative elementary volume
UC		Unit cell
Indices		
Subscripts		
b-y		blue–yellow
c		cell
cap		cap
cross		cross/two crossing cylinders
cub		cubic
curved		curved
eff		effective
half-cyl,30°		half cylinder cutout piece in a 30° angle
hex		hexagonal
i		inner
inter		intersection
m		mean
model		data obtained by the derived model
node		node
o		outer
planar		planar
r		radial domain
s		strut
S		solid
sim		data obtained by simulation
SRU		smallest repeatable unit
t		tube
tri		triangular
triple		planar triplet of cylinders
Ti		Titanium
vert		vertical
V		Volume
x		*x*-direction
y		*y*-direction
z		*z*-direction/axial domain
*		modification
Superscripts		
*		modification

Acknowledgements

This work was funded by the Deutsche Forschungsgemeinschaft (DFG, German Research Foundation)—432515505.

Open Access funding enabled and organized by Projekt DEAL.

Conflict of Interest

The authors declare no conflict of interest.

Author Contributions

Dominik Rudolf: Conceptualization (equal); Data curation (lead); Formal analysis (lead); Investigation (lead); Methodology (lead); Project administration (supporting); Software (lead); Validation (lead); Visualization (lead); Writing—original draft (lead); Writing—review and editing (lead). **Alexander Fink**: Conceptualization (equal); Formal analysis (supporting); Investigation (supporting); Methodology (supporting); Project administration (supporting); Software (supporting); Supervision (supporting); Validation (supporting); Visualization (supporting); Writing—review and editing (supporting). **Carolin Körner**: Conceptualization (supporting); Funding acquisition (equal); Project administration (equal); Supervision (supporting); Writing—review and editing (supporting). **Hannsjörg Freund**: Conceptualization (supporting); Funding acquisition (lead); Methodology (supporting); Project administration (supporting); Resources (lead); Supervision (lead); Visualization (supporting); Writing—review and editing (supporting).

Data Availability Statement

The data that support the findings of this study are available from the corresponding author upon reasonable request.

Keywords

auxetic structures, effective heat conductivity, periodic open cellular structures, process intensification, structured catalysts

Received: July 20, 2024
Revised: October 23, 2024
Published online: November 20, 2024

[1] A. Nazir, K. M. Abate, A. Kumar, J.-Y. Jeng, *Int. J. Adv. Manuf. Technol.* **2019**, *104*, 3489.
[2] A. Inayat, J. Schwerdtfeger, H. Freund, C. Körner, R. F. Singer, W. Schwieger, *Chem. Eng. Sci.* **2011**, *66*, 2758.
[3] L. Eckendörfer, D. Rudolf, A. Brix, M. Börnhorst, H. Freund, *Annu. Rev. Chem. Biomol. Eng.* **2024**, *15*, 163.
[4] C. Busse, H. Freund, W. Schwieger, *Chem. Eng. Process. Process Intensif.* **2018**, *124*, 199.
[5] M. Ambrosetti, G. Groppi, W. Schwieger, E. Tronconi, H. Freund, *Chem. Eng. Process. Process Intensif.* **2020**, *155*, 108057.
[6] R. Balzarotti, M. Ambrosetti, M. Arnesano, A. Anglani, G. Groppi, E. Tronconi, *Appl. Catal., B* **2021**, *283*, 119651.
[7] C. Busse, Dissertation, Friedrich-Alexander-Universität Erlangen-Nürnberg, Germany **2020**.
[8] L. Fratalocchi, G. Groppi, C. G. Visconti, L. Lietti, E. Tronconi, *Chem. Eng. J.* **2020**, *386*, 123988.

[9] L. Fratalocchi, G. Groppi, C. G. Visconti, L. Lietti, E. Tronconi, *Catal. Today* **2022**, *383*, 15.
[10] C. Busse, H. Freund, W. Schwieger, *Chem. Eng. J.* **2024**, *489*, 151139.
[11] F. Kapteijn, J. A. Moulijn, *Catal. Today* **2022**, *383*, 5.
[12] E. Bianchi, W. Schwieger, H. Freund, *Adv. Eng. Mater.* **2016**, *18*, 608.
[13] M. Bracconi, M. Ambrosetti, M. Maestri, G. Groppi, E. Tronconi, *Chem. Eng. Process. Process Intensif.* **2020**, *158*, 108169.
[14] K. Dubil, H. Wolf, T. Wetzel, B. Dietrich, *Int. J. Heat Mass Transfer* **2022**, *183*, 122083.
[15] X. Bai, A. Nakayama, *Appl. Therm. Eng.* **2019**, *160*, 114011.
[16] R. Hubert, O. Bou Matar, J. Foncin, P. Coquet, D. Tan, H. Li, E. H. T. Teo, T. Merlet, P. Pernod, *Int. J. Heat Mass Transfer* **2021**, *176*, 121364.
[17] P. Ranut, *Appl. Therm. Eng.* **2016**, *101*, 496.
[18] S. Stallard, H. Jiang, Y. Chen, T. L. Bergman, X. Li, *Mater. Des.* **2023**, *231*, 112027.
[19] M. Lämmermann, G. Horak, W. Schwieger, H. Freund, *Chem. Eng. Process. Process Intensif.* **2018**, *126*, 178.
[20] C. Ferroni, M. Bracconi, M. Ambrosetti, M. Maestri, G. Groppi, E. Tronconi, *Ind. Eng. Chem. Res.* **2021**, *60*, 10522.
[21] S. Trunk, A. Brix, H. Freund, *Chem. Eng. Sci.* **2021**, *244*, 116768.
[22] G. Littwin, S. Röder, H. Freund, *Ind. Eng. Chem. Res.* **2021**, *60*, 6753.
[23] K. Dubil, T. Wetzel, B. Dietrich, *Int. J. Heat Mass Transfer* **2023**, *200*, 123546.
[24] S. Razza, T. Heidig, E. Bianchi, G. Groppi, W. Schwieger, E. Tronconi, H. Freund, *Catal. Today* **2016**, *273*, 187.
[25] E. Bianchi, G. Groppi, W. Schwieger, E. Tronconi, H. Freund, *Chem. Eng. J.* **2015**, *264*, 268.
[26] I. G. Masters, K. E. Evans, *Compos. Struct.* **1996**, *35*, 403.
[27] C. Körner, Y. Liebold-Ribeiro, *Smart Mater. Struct.* **2015**, *24*, 025013.
[28] J. van Humbeeck, *Adv. Eng. Mater.* **2001**, *3*, 837.
[29] V. Buljak,G. Ranzi, in*Constitutive Modeling of Engineering Materials* (Eds: V. Buljak, G. Ranzi, In V. Buljak, G. Ranzi), Vol. *1*, Academic Press, **2021**, pp. 293–313.
[30] C. Körner, *Int. Mater. Rev.* **2016**, *61*, 361.
[31] Z. Fu, C. Körner, *Eur. J. Mater.* **2022**, *2*, 54.
[32] J. Schwerdtfeger, P. Heinl, R. F. Singer, C. Körner, *Phys. Status Solidi B* **2010**, *247*, 269.
[33] J. Schwerdtfeger, F. Wein, G. Leugering, R. F. Singer, C. Körner, M. Stingl, F. Schury, *Adv. Mater.* **2011**, *23*, 2650.
[34] L. Yang, O. Harrysson, H. West, D. Cormier, *Acta Mater.* **2012**, *60*, 3370.
[35] L. Yang, O. Harrysson, D. Cormier, H. West, H. Gong, B. Stucker, *JOM* **2015**, *67*, 608.
[36] F. Warmuth, F. Osmanlic, L. Adler, M. A. Lodes, C. Körner, *Smart Mater. Struct.* **2017**, *26*, 025013.
[37] Q. Zhou, M. D. Hayat, G. Chen, S. Cai, X. Qu, H. Tang, P. Cao, *Mater. Sci. Eng., A* **2019**, *744*, 290.
[38] P. Krooß, C. Lauhoff, T. Gustmann, T. Gemming, C. Sobrero, F. Ewald, F. Brenne, T. Arold, M. Nematolahi, M. Elahinia, J. Thielsch, J. Hufenbach, T. Niendorf, *Shape Mem. Superelasticity* **2022**, *8*, 452.
[39] A. Fink, Z. Fu, C. Körner, *Materialia* **2023**, *30*, 101823.
[40] Z. Lin, K. B. Surreddi, C. Hulme, S. Dadbakhsh, A. Rashid, *Adv. Eng. Mater.* **2023**, *25*, 12.
[41] A. Fink, D. Rudolf, B. Wahlmann, H. Freund, C. Körner, *Adv. Eng. Mater.* **2024**, *26*, http://doi.org/10.1002/adem.202401310.
[42] V. V. Calmidi, R. L. Mahajan, *J. Heat Transfer* **1999**, *121*, 2.
[43] COMSOL, Multiphysics Version 6.1: Documentation and Reference Manual, http://www.comsol.com **2022**.
[44] A. J. Otaru, R. O. Isa, A. U. Emene, A. A. Faruq, P. O. Sedemogun, S. M. Hassan, *Results Eng.* **2022**, *15*, 100531.
[45] S. Wang, Y. Jiang, J. Hu, X. Fan, Z. Luo, Y. Liu, L. Liu, *Comput.-Aided Des.* **2022**, *142*, 103123.
[46] J. Frochte, in *Finite-Elemente-Methode: Eine praxisbezogene Einführung mit GNU Octave/MATLAB*, Fachbuchverlag Leipzig im Carl Hanser Verlag, München, Germany, **2016**.
[47] Panua Technologies Sagl, Panua-Pardiso, https://panua.ch/.
[48] M. Klumpp, A. Inayat, J. Schwerdtfeger, C. Körner, R. F. Singer, H. Freund, W. Schwieger, *Chem. Eng. J.* **2014**, *242*, 364.
[49] A. Fink, B. Wahlmann, C. Körner, *Adv. Mater. Sustainable Manuf.* **2024**, *1*, 10004.
[50] J. N. Grima, D. Attard, B. Ellul, R. Gatt, *Cell. Polym.* **2011**, *30*, 287.
[51] A. Pietschak, A. G. Dixon, H. Freund, *Chem. Eng. Sci.* **2020**, *220*, 115614.